

To appear in Journal of Geophysical Research, 2000.

Dynamical Climatology of the LaRC Interactive Modeling Project for Atmospheric Chemistry and Transport (IMPACT) model

R. Bradley Pierce, Jassim A. Al-Saadi, Richard S. Eckman, T. Duncan Fairlie, William L. Grose, Mary M. Kleb, Murali Natarajan, and Jennifer R. Olson

NASA Langley Research Center, Hampton, Va

Submitted to JGR, December 15, 1999

Revised March 31, 2000

Short Title: Dynamical Climatology of the LaRC IMPACT model

Abstract: A comparison of the NASA Langley Research Center (LaRC) Interactive Modeling Project for Atmospheric Chemistry and Transport (IMPACT) model's dynamical characteristics with assimilated data sets and observations is presented to demonstrate the ability of the model to represent the dynamical characteristics of Earth's troposphere and stratosphere. The LaRC IMPACT model is a coupled chemical/dynamical general circulation model (GCM) of the Earth's atmosphere extending from the surface to the lower mesosphere. It has been developed as a tool for assessing the effects of chemical, dynamical, and radiative coupling in the stratosphere on the Earth's climate. The LaRC IMPACT model winds and temperatures are found to be in fairly good agreement with Upper Atmospheric Research Satellite (UARS) United Kingdom Meteorological Office (UKMO) assimilated winds and temperatures in the lower stratosphere. The model upper stratospheric zonal mean temperatures are also in good agreement with the UARS-UKMO climatology except for a cold winter pole which results from the upward extension of the cold vortex temperatures and an elevated winter stratopause in the model. The cold pole bias is consistent with the overprediction of the winter stratospheric jet strength, and is characteristic of stratospheric GCMs in general. The model northern and southern hemisphere stratospheric eddy heat and momentum fluxes are within the expected interannual variability of the UARS-UKMO climatology. The combined effects of water vapor transport, radiative, convective, and planetary boundary layer parameterizations are shown to produce tropospheric winds and circulation statistics that are in good agreement with the UARS-UKMO climatology, although the model tropopause and upper tropospheric temperatures are generally cold relative to the UARS-UKMO temperatures. Comparisons between the model and UARS-UKMO climatology indicate that the model does a reasonable job in reproducing the frequency of observed synoptic-scale storms during the northern and southern hemisphere winters. Generally good agreement is found between the model and observations in the distribution of outgoing longwave radiation and precipitable water. However, the model precipitation and cloud distributions are influenced by spectral truncation errors which indicate that the T32 spectral resolution of the model is probably not adequate to accurately represent coupling between localized convection and large-scale water vapor transport. The agreement between the observed and model stratospheric circulation and temperatures, reasonableness of the model stratospheric wave driving, and stability of the model climatology provides confidence that the LaRC IMPACT model is appropriate for multi-year coupled radiation/chemistry/dynamics studies of the stratosphere.

Introduction

Atmospheric modeling and simulation studies are important tools for understanding the fundamental processes of radiation, chemistry, and dynamics that determine the circulation, thermal structure, and distribution of constituents in the Earth's atmosphere. Many of these studies have treated these processes independently or have suppressed important couplings between the processes. This approach was a conscious strategy adopted to make the studies tractable and often relied on assumptions that the couplings were weak enough to neglect. Recently however, there has been increased awareness that many phenomena of interest involve subtle and complex interactions among these processes. In the stratosphere, notable examples include the annual formation and decay of the Antarctic ozone hole [Farman et al., 1985] and the downward trend in mid-latitude ozone in the lower stratosphere [Stolarski et al., 1991]. At the same time, there has been increased emphasis on global change studies which attempt to assess long-term (decadal or longer) impact on the Earth's atmosphere from both anthropogenic and natural changes. Clearly, these studies must rely on simulation models that incorporate all of the relevant processes and correctly represent the interactions between those processes.

The NASA Langley Research Center (LaRC) Interactive Modeling Project for Atmospheric Chemistry and Transport (IMPACT) model has been developed as a tool for assessing the effects of stratospheric chemical, dynamical, and radiative coupling on the Earth's climate. In this paper we present a comparison of the model's dynamical characteristics with assimilated data sets and observations to demonstrate the ability of the model to represent the dynamical characteristics of the Earth's atmosphere. The fidelity of the model's simulation of the chemical characteristics of the atmosphere will be presented elsewhere. The intent of these comparisons is to establish a base-line model simulation which will be used, in conjunction with ongoing simulations, to characterize the impact of natural processes (i.e. volcanic eruptions, El Nino/Southern Oscillation, Quasi-Biennial Oscillation) on interannual variability in stratospheric dynamics and chemistry. These studies are designed to characterize the processes responsible for the natural variability in the Earth-Atmosphere system and are necessary precursors to investigations which explore the impact of anthropogenic processes (such as reductions in CFC emissions due to the Montreal Protocol) on the photochemistry and dynamics of the stratosphere.

A number of General Circulation Models (GCMs) which include a fully resolved stratosphere have been developed over the last decade. Thirteen of these models, including the LaRC

IMPACT model, participated in the recent World Climate Research Program (WCRP) Stratospheric Processes and their Role in Climate (SPARC) GCM-reality Intercomparison Project for SPARC (GRIPS) [Pawson, et al., 2000]. This intercomparison was designed to examine model simulations of the coupled troposphere-middle atmosphere system and document the relative strengths and weaknesses of the participating models. The IMPACT model is unique among the middle-atmospheric models evaluated in GRIPS in that it includes comprehensive stratospheric ozone photochemical calculations. (Two other GRIPS models include coupled chemistry/radiation calculations but with simplified ozone photochemistry.) The additional computational resources required for the photochemical calculations dictates that simplifications must be made in some of the physical parameterizations within the LaRC IMPACT model. The consequences of these simplifications will be discussed in the context of relevant comparisons of LaRC IMPACT model results with climatology and with some of the models participating in the GRIPS study.

Section 1 of this paper provides a description of the model and discusses improvements in the current model relative to previous versions. Section 2 presents an overview of a 5 year coupled simulation. Section 3 documents comparisons between the model dynamical fields and observed and other models climatologies. Section 4 compares the model tropospheric radiative distributions and moisture diagnostics with observed climatologies, and Section 5 presents a summary of the comparisons and conclusions.

1) Model Description

The LaRC IMPACT model is a global, three-dimensional general circulation model (GCM) of the troposphere, stratosphere and mesosphere with coupled dynamics, chemistry and radiation. The dynamics component of the model traces its heritage to the model originally described by Hoskins and Simmons [1975]. The complexity of the model has evolved over the years as it was used for studies of atmospheric dynamics, chemistry and transport [e.g. Grose et al., 1984, Grose et al., 1987, Blackshear et al. 1987, Pierce et al. 1993]. The chemistry component of the model is derived from the chemical transport model (CTM) described by Eckman et al., [1995, 1996]. Recently, these models have been merged into an interactive model which predicts the combined dynamical, radiative and chemical evolution of the Earth's atmosphere. Dynamical coupling occurs through radiative and transport processes and is accomplished by using the computed three-dimensional ozone distribution in the stratospheric radiative heating calculations. In

addition to this coupling, other significant improvements have been incorporated into the model which allow us to conduct realistic multi-year coupled simulations.

The mass and momentum budgets of the model are expressed in terms of log of surface pressure, vorticity and divergence tendency equations. The thermodynamic state of the atmosphere is governed by temperature and specific humidity tendency equations, while the chemical state of the atmosphere is determined by mass continuity equations for 24 chemical constituents and families. The terrain-following sigma coordinate [Phillips, 1957] is used throughout the model domain. The model fields are represented by truncated sums of spherical harmonics. Triangular truncation is employed to 32 waves in the longitudinal and meridional directions (T32). This is twice the resolution used in previous versions of the model. Pseudo-spectral transport is used in the horizontal. The transform method, described by Orszag [1970] and Eliassen et al. [1970], is used to transform variables to a Gaussian grid of approximately 2.8 degrees of longitude by 2.8 degrees of latitude in order to compute product terms in the governing equations and for parameterization of physical and photochemical sources and sinks. The vertical domain of the model has been extended from the 24 level (surface to 60km) resolution used in previous versions of the model to 34 levels (surface to 90km) for dynamical calculations. Model levels are approximately 100 hPa apart in the troposphere and about 3 km apart in the stratosphere. Explicit chemical calculations extend to approximately 60 km (the top 10 levels of the dynamical variables are averaged to define temperature and winds in the top layer of the chemical module). The thick top layer of the chemical module is chosen primarily because upper mesospheric chemistry is not fully accounted for in the model. A third-order upwind biased, flux limited scheme [Anderson, 1986] is used for vertical transport. A spectrally smoothed representation of the Earth's topography is used at the lower boundary. The dynamical component uses the semi-implicit integration scheme of Robert et al. [1972]. Leapfrog timestepping is applied to the chemical constituent fields. A 15-minute timestep is used for horizontal resolution T32. A 1-2-1 time filter is applied every six timesteps to control time splitting.

Significant improvements in the model troposphere have been made since the work of Pierce et al. [1993], which used a prescribed distribution of climatological heating rates in the troposphere based on isentropic mass budget calculations [Johnson et al., 1989]. The model now includes water vapor transport and parameterizations of tropospheric physical processes. Given the complexity of developing a middle atmosphere coupled chemistry/dynamics/radiation model, we have

chosen to use simple, albeit primitive, physical parameterizations. The parameterization of latent heat release due to large-scale moisture convergence is an extension of the Kessler [1969] scheme used by Zapotocny et al. [1991]. Large-scale condensation rates (K_{cond}) are a function of specific humidity (q) and pressure (p)

$$K_{\text{cond}} = (r(p) \times s(q)) / (dt)$$

where:

$$r(p) = 0.1 + \frac{\left(e^{\left(1 - \frac{p-300}{p_{\text{sfc}}-300} \right)^3} - 1 \right)}{e^1 - 1}$$

and:

$$s(q) = (q - q_0) / (q_1 - q_0)$$

The term $r(p)$ is constrained to remain within 0.1 and 1.0 and the term $s(q)$ is constrained to remain between 0.0 and 1.0. Large-scale condensation occurs whenever the specific humidity within a grid-box is greater than the threshold specific humidity (q_0). Large-scale evaporation of falling rain occurs instantaneously ($K_{\text{evap}} = dt^{-1}$) whenever the specific humidity within a grid-box is less than the threshold specific humidity (q_1). In the current simulation, q_0 and q_1 correspond to 80% and 100% relative humidity, respectively. The large-scale precipitation scheme was developed to account for low intensity rain events (drizzle) associated with low level, nonconvective cloud systems and allows the large-scale precipitation to develop gradually in response to large-scale moisture convergence. The formulation of large-scale precipitation allows for supersaturated airmasses. The amount of water vapor remaining in a grid-box in excess of q_0 is diagnosed as cloud liquid water. The large-scale cloud fraction is a linear function of the grid-box relative

humidity ranging from 0.25 to 1.0 for relative humidities between 80% and 100%, and is fixed at 1.0 for relative humidities above 100%.

The moist convection scheme is based on that of Kuo [1974] with closure described by Molinari [1982]. The planetary boundary layer formulation is based on the scheme used in the Goddard Laboratory for Atmospheres (GLA) 4th-order GCM [Kalnay et al., 1983]. The water vapor distribution used in the moist convection scheme is constrained to be less than or equal to q_1 (i.e. the moist convection doesn't see supersaturated airmasses). Convective cloud fractions and liquid water content are fixed at 0.3 and $2.0 \times 10^{-6} \text{ gm cm}^{-3}$, respectively. The tropospheric radiative calculations use the sum of large-scale and convective amounts for both cloud fraction and liquid water content. The PBL is composed of a mixed layer and a surface layer. The flux of moist static energy into the surface layer is assumed to equal the flux out of the surface layer (zero flux gradient condition). As will be shown, the convective parameterization, coupled with the relatively coarse spectral resolution of the water vapor transport, leads to significant localized errors in the representation of precipitation. Furthermore, the PBL formulation tends to develop unrealistically warm ground temperatures during northern hemisphere (NH) summer and unrealistically cold ground temperatures during NH winter. To alleviate the PBL problem we impose a constraint which restricts the instantaneous ground temperature to be within 10K of the orographically adjusted climatological ground temperature from NASA GLA. Climatological ground temperatures equatorward of the northern and southern hemisphere snow lines are set to a minimum of 273.15K. Improvements in the representation of convective precipitation will likely require replacement of the current convective parameterization with more advanced (and computationally expensive) formulations.

The National Center for Atmospheric Research (NCAR) Community Climate Model Version 2 (CCM2) radiation scheme [Williamson et al., 1987] is used in the troposphere. In the stratosphere, radiative heating rates are computed using the radiative scheme of Shine [1987]. This scheme incorporates the absorption of solar UV radiation by ozone and molecular O_2 , and the infrared contributions due to CO_2 , H_2O and O_3 . The Shine scheme is applied from 100 hPa up to an altitude of approximately 80 km. Above 80 km, the diabatic heating is made to decline linearly to zero at 95 km. The model's chemistry and dynamics calculations are coupled through the Shine radiation scheme. The calculated stratospheric ozone distribution feeds back on the strato-

spheric temperature and wind fields through the solar and infrared calculations. Currently, there is no explicit interaction between the tropospheric and stratospheric radiation schemes. Instead, the Shine code uses its default calculation of upwelling tropospheric longwave and reflected short-wave fluxes (based on climatological 700 hPa temperatures and reflectance) and the tropospheric radiative calculations use a fixed ozone distribution. The computed stratospheric and tropospheric radiative heating rates are blended together at 100 hPa.

The parameterization of momentum deposition associated with sub-grid scale gravity waves is critical to the simulation of the mesospheric circulation [Andrews et al., 1987]. The mesospheric momentum deposition by gravity waves also plays a significant role in determining the circulation in the stratosphere, via “downward control” [Haynes et al., 1991]. Consequently, some type of orographic gravity wave drag is now commonly included in most middle atmospheric GCMs. This source of momentum deposition is primarily responsible for the deceleration of the stratospheric winter westerlies in the lower mesosphere and also helps reduce the “cold pole” bias found in most middle atmosphere GCMs. The McFarlane [1987] gravity wave drag scheme is used in the IMPACT model to represent the effects of orographically generated sub-grid scale gravity waves in the upper stratosphere/lower mesosphere. Orographic gravity wave parameterizations only consider stationary gravity waves and therefore do not account for the complete spectrum of small-scale waves in the atmosphere. The IMPACT model is similar to a number of other middle atmospheric GCMs [Boville, 1995; Beagley et al., 1997; Butchart and Austin, 1998] in that the impact of these non-stationary waves is represented with Rayleigh friction. Rayleigh friction is applied to both the zonal and planetary wave components of the flow. The Rayleigh friction also acts as a “sponge layer” to avoid spurious reflections at the top of the model. Additional damping includes bi-harmonic diffusion, which is applied to the model’s temperature, vorticity, divergence, water vapor and chemical constituent fields, and a nonlinear, time-split vertical diffusion scheme, based on the scheme used in the NCAR CCM2, which is applied to the temperature, momentum and moisture distributions to suppress tropical inertial instabilities.

The selection of the Rayleigh friction profile was dictated by the need to represent realistic lower stratospheric seasonal ozone evolution in polar latitudes. Polar ozone photochemistry is highly temperature dependent due to the model parameterizations of heterogeneous chemistry on polar stratospheric cloud (PSC) particles. Previous versions of the model used a Rayleigh friction coefficient which was zero below 5 hPa, followed the profile of Holton [1976] between 1 and 0.5

hPa, and then increased rapidly to a maximum damping rate of 2.0 days^{-1} at the top level of the model. This profile, when used in conjunction with the new explicit tropospheric physics, resulted in very little planetary activity during NH winter, a late final warming (mid-May), and NH lower stratospheric vortex temperatures which were consistently below the Type I PSC threshold. The combination of sustained cold vortex temperatures and a late final warming resulted in unrealistically high NH spring time ozone loss. A series of simulations were conducted to examine the sensitivity of the lower stratospheric circulation to the assumed Rayleigh friction profiles. We adopted the 2x Holton [1976] Rayleigh friction profile for the current simulations since this choice provided the best balance between warming the NH vortex enough without warming the southern hemisphere (SH) vortex too much in the lower stratosphere. The delicate balance between NH and SH vortex temperatures necessary to achieve reasonable simulations of polar ozone chemistry is due to the fact that the LaRC IMPACT model SH lower stratospheric temperatures tend to be slightly warmer than climatological temperatures during SH winter while the model NH lower stratospheric temperatures show a slight cold bias.

2) LaRC IMPACT model baseline simulation

A 5-year coupled model simulation, initialized on January 1st, has recently been completed. Initial conditions for this simulation were obtained from the 4th year of a cycle of developmental runs with earlier versions of the coupled model. The developmental runs were typically conducted for 1 to 2 years. Initial conditions for these earlier simulations came from a multi-year dynamics-only simulation which included on-line N_2O transport. Chemical initial conditions for the coupled runs were obtained from the transported N_2O by performing N_2O -potential temperature mapping of chemical species from a multi-year, 24-level, T16 off-line CTM simulation [Eckman et al., 1995]. After the first year of the current simulation, during which there was considerable adjustment in tropospheric ozone, the trend in total ozone was a less than 0.1% per year increase. Global mean temperatures remained very stable (decrease of 0.01% per year).

The model's primary application has been the middle stratosphere ($\sim 10 \text{ hPa}$) where large interannual variability exists. Plate 1 shows a comparison of timeseries of northern and southern hemisphere 10 hPa polar temperatures, zonal mean winds, and wave number 1 and 2 geopotential heights, for each of the five years of the model simulation with observations from a 6-year clima-

tology based on the United Kingdom Meteorological Office (UKMO) assimilation for the Upper Atmospheric Research Satellite (UARS) [Swinbank and O'Neill, 1994]. A 30-day running average has been applied to the observations. The absolute maximum and minimum polar temperatures, winds and wave number 1 and 2 heights on each day of the 6-year climatology are indicated by the shading. The UARS-UKMO assimilation uses the troposphere-stratosphere configuration of the UKMO Unified Model (UKMO-UM) [Cullen, 1993] and has been used extensively as a UARS correlative data set. We chose the relatively short UARS-UKMO climatology for comparison since the simulation is our benchmark for ongoing modeling studies which are focused on interpretation of stratospheric radiative/chemical/dynamical coupling during the UARS time period. Also, since the UARS-UKMO assimilation model extends to 0.4 hPa, we are able to compare winds, temperatures, heat and momentum fluxes in a fully self consistent manner instead of having to rely on geostrophic or balance assumptions to determine winds in the middle and upper stratosphere. The UARS-UKMO zonal mean temperatures, winds and residual mean circulation compare favorably with the Goddard Earth Observing System (GEOS 1) assimilation from the Goddard Data Assimilation Office (DAO), [Coy and Swinbank, 1997].

Model 10 hPa polar temperatures capture the observed seasonal cycle fairly well in the NH. The model minimum temperatures lag the observed minimum by approximately 1 month in the SH. Model deficiencies include a 10 to 20K cold bias in NH polar temperatures during January and February and a 5K cold bias during NH summer. Model SH polar temperatures are approximately 7K too cold during summer and 10 to 15K too cold during late winter to early spring. The simulation shows somewhat less variability in NH polar temperatures during January and February than is observed. The model NH variability is larger during the first and third year of the simulation with a minor warmings during February and March of year 1 and late February of year 3. Earlier final warmings occur during years 2 and 5. SH polar temperature variability is comparable to the observed variability and the model shows interannual variations in the timing of the SH final warming. The model NH 10 hPa winds are in very good agreement with the UARS-UKMO climatology at 60°N. Daily wind speeds lie within the observed daily maxima and minima except for May through July, where the model easterlies are somewhat weaker than observed. SH westerlies are significantly underestimated during the entire SH winter (April through September) at 60°S.

The amplitudes and degree of variability in the NH 10 hPa wave number 1 geopotential heights are consistent with the observations except for early winter (November through January), when wave amplitudes are generally lower than observed. Wave number 2 heights are in good agreement with observed amplitudes in the NH. The reduced NH wave number 1 activity during early winter is consistent with the colder polar temperatures, relative to the UARS-UKMO climatology, found during each year of the model simulation. The SH wintertime wave number 1 heights are significantly lower than observed and show less variability. The climatological amplitudes and variability of the SH wavenumber 2 heights are well represented in the model.

3) Comparisons with UARS-UKMO Climatology

In this section we focus on December-January-February (DJF) and June-July-August (JJA) comparisons of 4-year means (year 2 through year 5) of the model simulation to the UARS-UKMO climatology. Seasonal standard deviations of the UARS-UKMO climatology are used to provide an estimate of the observed interannual variability during the UARS time period. The agreement between the UARS-UKMO climatology and the 4-year model climatology is quantified by comparing differences between the model and observations to the expected interannual variability.

3.1) Zonal Mean U Wind

The model DJF zonal mean winds for years 2-5 of the simulation are compared with the UARS-UKMO climatology in Figure 1. The climatological NH stratospheric jet tilts equatorward with height reaching over 50ms^{-1} at 0.4 hPa, 45°N . DJF standard deviations reflect interannual variability in the NH jet and range from 2ms^{-1} in the lower stratosphere to over 6ms^{-1} at 1 hPa. The peak interannual variability in the tropics is associated with the observed Quasi-biennial Oscillation (QBO), which is not present in the model. The model NH stratospheric jet shows a 60ms^{-1} maximum at 70°N near 1 hPa. The lack of an equatorward tilt of the model jet maximum with altitude results in differences of 30ms^{-1} at 70°N which are larger than four standard deviations from the mean UARS-UKMO climatology (shaded regions in lower left panel) and therefore larger than would be expected from interannual variability. The model jet strength is within 5ms^{-1} of the UARS-UKMO climatology in the NH lower stratosphere. The observed SH easter-

lies extend from the tropical tropopause up to 0.4 hPa (the top of the UARS-UKMO data set) with a peak of over 50ms^{-1} . The model SH easterlies are generally 5ms^{-1} weaker than climatology throughout the SH stratosphere. This westerly bias is larger than would be expected from interannual variability, which is quite low within the easterly jet. The strength and location of the tropospheric NH jet maximum is in very good agreement with the observed jet. The strength of the SH tropospheric jet maximum agrees with climatology but the model jet is centered about 10° equatorward of the observed jet maximum. The resulting dipole difference pattern of 5 to 10ms^{-1} is larger than would be expected from interannual variability. A slight westerly bias is evident in the model lower tropical troposphere.

The model JJA zonal mean winds for years 2-5 of the simulation are compared with the UARS-UKMO climatology in Figure 2. The observed SH stratospheric jet reaches a maximum of over 80ms^{-1} at 10 hPa and extends up to 0.4 hPa, tilting equatorward with height. Stratospheric westerlies extend down below 100 hPa poleward of 50°S resulting in a double jet structure in the SH upper troposphere/lower stratosphere. Interannual variations of the SH stratospheric westerlies are 2 to 4ms^{-1} poleward of 50°S and greater than 8ms^{-1} on the equatorward flank of the jet. The model SH stratospheric westerlies peak at 100ms^{-1} and show a slight poleward tilt with height above 10 hPa. The model lower stratospheric SH westerlies are $15\text{-}25\text{ms}^{-1}$ weaker than observed. The differences between the model and observed SH stratospheric westerlies are primarily associated with weaker vertical wind shear poleward of 50°S in the upper troposphere/lower stratosphere and a poleward instead of equatorward tilt with height in the upper stratosphere of the model. The NH stratospheric easterlies are within 5ms^{-1} of the observed easterlies in the upper stratosphere. The observed extension of the summertime easterlies into the tropics at 10 hPa is weak in the model winds, resulting in differences of up to 10ms^{-1} . The strength and location of the tropospheric JJA jet is proper in the SH while the NH tropospheric jet is displaced equatorward relative to the observed jet resulting in $5\text{-}10\text{ms}^{-1}$ differences which are larger than can be expected from interannual variability. There is a tropical westerly bias in the JJA period which is larger than that found during DJF.

Pawson et al. [2000] presents comparisons between January zonal mean balanced winds obtained from NCEP geopotential height analyses and the 13 GRIPS middle atmosphere models.

The quality of the LaRC IMPACT simulation of the NH polar night jet falls well within the range of that found in the other GRIPS models. The separation between the subtropical and polar night jet (which is captured quite well in the LaRC IMPACT model) is accomplished to varying degrees in the models used in the GRIPS intercomparison. The lack of an equatorward tilt of the winter westerlies in the upper stratosphere of the LaRC IMPACT model is typical of most of the GRIPS models, which also show large variations in the strength of the NH stratospheric jet in the upper stratosphere. Pawson concluded that the ability to properly simulate the upper stratospheric NH jet was not clearly related to either model resolution or the nature of the gravity wave parameterizations considered in the GRIPS intercomparison. This is in contrast with the results of Rind et al., [1988] who found significant improvements in the simulation of the upper stratospheric polar night jet in both hemispheres in the Goddard Institute for Space Studies (GISS) Global Climate-Middle Atmosphere Model (GCMAM) when parameterizations of the full spectrum of orographic, convective, and shear-induced gravity wave momentum deposition were included. In particular, the GISS model with a spectrum of gravity wave momentum sources captured the observed equatorial tilt and peak strength of the NH and SH jets quite well above 1hPa. This altitude region was not considered in the GRIPs intercomparison.

The maximum strength of the SH JJA polar night jet ($\sim 100 \text{ms}^{-1}$) in the LaRC IMPACT model is in better agreement with climatology than some middle atmospheric models of comparable resolution. For example, the Geophysical Fluid Dynamics Laboratory SKYHI Troposphere-Stratosphere-Mesosphere model [Hamilton, et al, 1995] (which does not include either Rayleigh friction or orographic gravity wave drag) has peak SH JJA winds in excess of 150ms^{-1} for $3^\circ \times 3.6^\circ$ and $2^\circ \times 2.4^\circ$ resolutions and in excess of 120ms^{-1} for $1^\circ \times 1.2^\circ$ resolution. The Middle Atmosphere version of the National Center for Atmospheric Research Community Climate Model 2 (MACCM2) [Boville, 1995] (which uses the same orographic gravity wave parameterization as the LaRC IMPACT model but an approximately 50% weaker Rayleigh friction profile below 0.01 hPa) has peak SH July winds in excess of 150ms^{-1} for T42 and T63 resolutions and 125ms^{-1} for T106 resolutions. The Middle Atmosphere version of the UKMO-UM [Butchart and Austin, 1998] (which uses a gravity wave drag parameterization below 20 hPa and strong Rayleigh friction above 20 hPa) has peak July SH winds which are between 90 and 100ms^{-1} , depending on whether the Rayleigh friction is approximately 2 or 3 times stronger than used in the LaRC

IMPACT model . The GISS GCMAM model [Rind et al., 1988] (which uses no Rayleigh friction but includes a complete spectrum of parameterized gravity waves) has peak JJA SH winds of 90ms^{-1} .

It is clear from these examples that there is a wide range of approaches to representing the effects of unresolved scales on the momentum budget of the upper stratosphere. What is not clear at this time is which approach provides better simulations of the observed polar night jets. The explicit representation of the spectrum of gravity waves (as in the GISS model) is more physically based than Rayleigh friction. And, as pointed out by Shepherd et al. [1996], interactions between gravity wave drag and Rayleigh friction can lead to artificial couplings between the upper and lower level dynamics. On the other hand, there is little observational basis for many of the assumptions required to parameterize the full spectrum of gravity waves. Surprisingly, the UKMO-UM, GISS GCMAM, and LaRC IMPACT SH jet structures are very similar in spite of the large differences in the treatment of upper stratospheric momentum deposition.

3.2) Zonal Mean Temperature

The model DJF zonal mean temperatures for years 2-5 of the simulation are compared with the UARS-UKMO climatology in Figure 3. The observed upper tropospheric/lower stratospheric SH polar temperatures are nearly isothermal at 230 K. Observed stratospheric temperatures then increase gradually with altitude until 10 hPa, where the lapse rate increases significantly. The model SH polar tropopause temperatures are near 220 K, resulting in a 10 K difference between the observed and modeled temperatures poleward of 50°S at 100 hPa. However, the model lapse rate is larger than observed so that temperatures agree with observations at the SH stratopause. Both the observed and modeled SH stratopause temperatures reach a peak of 280 K near 1 hPa. The UARS-UKMO stratopause remains at nearly the same altitude throughout the tropics and into the NH with gradually decreasing temperatures. The UARS-UKMO stratopause temperatures reach a secondary peak of 250K between 1 hPa and 0.6 hPa at the north pole. The modeled stratopause temperatures are consistent with the UARS-UKMO temperatures except for northward of 50°N , where the LaRC IMPACT model shows an elevated NH winter stratopause with peak temperatures of 260 K. This rise in the stratopause height contributes to the dipole pattern in the difference field at the north pole with an amplitude of near 20 K. This dipole

difference pattern is larger than expected from interannual variability in this region. Climatological temperatures compiled by Chandra et al., [1990] which include temperatures generated by Barnett and Corney, [1985] (not shown) suggest that this rise in the altitude of the model stratopause at the north pole is a real feature which is apparently not captured in the UARS-UKMO assimilated temperatures, most likely due to the proximity of this feature to the top of the assimilation model. Model polar temperatures in the NH middle to upper stratosphere are 5 to 10K colder than the observed temperatures and also contribute to the dipole difference pattern. The middle stratosphere (10 hPa) is where the maximum interannual variability is found in the observed zonal mean temperature field. The 5 to 10K model cold bias in this region is within the expected interannual variability of the DJF mean temperature. Throughout the rest of the stratosphere the model temperatures are within 2.5-5K of the observed temperatures. The model tropopause temperatures are 5-10K colder than observed tropopause temperatures. Model temperatures are also more than 5K colder than the UARS-UKMO climatology in the middle troposphere. This tropopause and middle tropospheric cold bias is significantly larger than the observed interannual variability in this region, which is quite small.

The model JJA zonal mean temperatures for years 2-5 of the simulation are compared with the UARS-UKMO climatology in Figure 4. Both the observed and modeled JJA zonal mean temperatures are nearly anti-symmetric to their DJF counterparts, except that temperatures within the SH polar stratosphere are colder and the interannual variability is less. The largest JJA differences are similar to, but larger than, their DJF counterparts. These differences are associated with the upward extension of the coldest polar temperatures in the model SH vortex and the biases in the altitude of the winter stratopause in the UARS-UKMO assimilation. In the lowermost stratosphere (below 70 hPa), the model SH polar temperatures are slightly warmer than observed (<5K). This relatively small difference is still more than expected from interannual variability from the climatological JJA temperatures, which show very little interannual variability during the UARS time period. The model middle stratospheric temperatures are within 2.5-5K of the observed temperatures. The JJA tropopause and upper troposphere cold bias is of similar magnitude to that found in DJF.

The 15-20K NH and 25K SH winter cold pole biases found between 10 and 1 hPa in the LaRC IMPACT model are of similar magnitude to those found in other middle atmosphere models with similar resolutions [Rind et al., 1988, Boville, 1995; Hamilton et al, 1995; Butchart and

Austin, 1998]. The 2.5-5K cold bias found elsewhere in the middle and upper stratosphere is generally less than that found in other comparable middle atmosphere models [Hamilton et al, 1995; Butchart and Austin, 1998]. The LaRC IMPACT model's 5-10K tropopause and 5K upper tropospheric cold biases are considerably larger than those found in most other middle atmospheric models [Pawson et al, 2000].

3.3) Zonal Mean Eddy Momentum and Heat Fluxes

Figure 5 shows DJF total eddy momentum fluxes ($\overline{u'v'}$) for the UARS-UKMO climatology and the model. These diagnostics serve to illustrate the fidelity of the model stationary and transient eddies and also indicate the strength of the zonal mean momentum forcing by the eddies. The observed NH stratospheric poleward (+) momentum fluxes reach amplitudes of over 400 m^2s^{-2} at 55°N near the top of the UARS-UKMO data set. There is considerable interannual variability in the observed stratospheric momentum fluxes reflecting year-to-year variations in NH planetary-wave activity. The model momentum fluxes show a somewhat weaker peak of 320 m^2s^{-2} at 60°N near 0.5 hPa and then decrease with altitude above that level. Differences between the modeled and observed stratospheric momentum fluxes are primarily associated with a poleward displacement of the maximum in the modeled momentum flux and are generally within the expected interannual variability. The pattern of the observed tropospheric eddy momentum fluxes is associated with eddy momentum flux convergence near the tropospheric zonal mean jet maxima. This momentum flux convergence is a well known feature of mature baroclinic eddies and provides a momentum source for the zonal mean tropospheric jets. Interannual variability in the location of the eddy flux convergence accounts for most of the observed variability. The location and strength of the model tropospheric momentum fluxes agree with observations except for weaker poleward eddy momentum flux in the core of the SH tropospheric jet. This results in differences between the modeled and observed SH poleward flux of $-40\text{m}^2\text{s}^{-2}$ at 50°S which is larger than would be expected from interannual variations.

Figure 6 shows JJA total eddy momentum fluxes for the UARS-UKMO climatology and the model. The observed poleward (-) momentum flux in the SH winter is significantly less than its NH counterpart, reflecting the lack of large-amplitude planetary wave activity in the SH winter stratosphere. Still, relatively large interannual variability is found at these altitudes. The model

poleward momentum flux is weaker than is observed although still within the expected interannual variability over most of the region. The observed JJA tropospheric eddy momentum fluxes are anti-symmetric with respect to the DJF fluxes, reflecting the increased baroclinic eddy activity and enhanced momentum flux convergence near the SH winter jet and decreased eddy momentum flux convergence near the NH summer jet. The modeled JJA eddy momentum fluxes show similar patterns but are weaker than observed in the northern and southern hemisphere jet cores.

Figure 7 shows DJF total eddy heat fluxes ($\overline{v't'}$) for the UARS-UKMO climatology and the model. These diagnostics indicate the strength of the poleward eddy heat transport. The observed stratospheric eddy heat flux shows a peak of 160Kms^{-1} at 60°N below 1 hPa and then decays above this altitude. The model stratospheric eddy heat flux peaks at 190Kms^{-1} at 70°N near 1 hPa. Differences between the model and observed eddy heat fluxes are primarily associated with the upward extension of the model eddy heat fluxes and are within the expected interannual variability of the UARS-UKMO climatology. The pattern in the observed DJF tropospheric eddy heat fluxes is consistent with poleward heat flux by amplifying baroclinic eddies, with peaks near the surface and at the middle latitude tropopause. The apparent discontinuity at 50°N near 200 hPa in the observed eddy heat fluxes is likely due to the relatively coarse vertical resolution of the UARS pressure levels which are used for the UARS-UKMO assimilated data in the troposphere. The modeled tropospheric eddy heat fluxes tend to overestimate the strength of the heat flux in the middle troposphere and underestimate the amplitude of the eddy heat flux at the tropopause by $4\text{-}12\text{Kms}^{-1}$.

Figure 8 shows JJA total eddy heat fluxes for the UARS-UKMO climatology and the model. The model and observed stratospheric eddy heat fluxes both show peaks in the upper stratosphere of over 60Kms^{-1} at 60°S . The expected interannual variability is relatively large compared to the amplitude of the SH climatological heat flux. The model underestimates the JJA poleward heat flux at the SH middle latitude tropopause and overestimates the surface poleward heat flux at NH middle latitudes.

3.4) Transformed Eulerian Mean (TEM) Circulation

To compare the observed and modeled TEM circulations, we computed daily TEM streamfunctions from vertical integrals of observed and model residual mean meridional veloci-

ties (\bar{v}^*) [Andrews et al., 1987] and then time-averaged the daily values to obtain seasonal means. A zero TEM streamfunction boundary condition was imposed at the uppermost assimilation and model levels. Model sigma-coordinate meridional velocities and temperatures were interpolated to pressure surfaces for the calculation.

Figure 9 shows the DJF TEM streamfunction obtained from the UARS-UKMO assimilation and the model. Both the observed and modeled TEM streamfunctions show the familiar Brewer-Dobson circulation with a dominant NH wintertime branch (+) and a weaker SH branch (-). The modeled TEM streamfunction is generally smoother than is observed and extends higher in altitude. The reduced vertical extent of the UARS-UKMO TEM streamfunction is a consequence of imposing the zero boundary condition at 0.4 hPa, the top of the UARS-UKMO assimilation. The UARS-UKMO TEM streamfunction shows small scale circulation cells at 5 hPa in the SH subtropics and 70 hPa in NH midlatitudes. The origin of the circulation anomalies is not clear. However, the January UARS-UKMO TEM streamfunction shown in Butchart and Austin [1998] shows nearly identical features. Butchart and Austin also found similar, although less pronounced, features in the UKMO-UM model TEM streamfunction. They suggested that deficiencies in the assimilation model were corrupting the UARS-UKMO assimilated TEM streamfunction. Consequently, it is likely that the circulation anomalies in the UARS-UKMO TEM streamfunction are not real. The equatorial discontinuity in the model TEM streamfunction at 100 hPa is due to the relatively coarse vertical resolution of the pressure-interpolated model data set.

Tropical ascent due to diabatic heating within the Inter-Tropical Convergence Zone (ITCZ) is associated with strong meridional gradients of the tropospheric TEM streamfunction and occurs near 10°S in both observations and the model. The observed and modeled ascending branch of the Brewer-Dobson circulation extends to near 70 hPa before the northern and southern hemisphere circulations split. The model shows more uniform poleward and downward sloping streamfunction contours than are observed, resulting in a reduction in the depth of the region of strong descent over the poles. However, the sharp descent of the UARS-UKMO TEM streamfunction may be an artifact of the polar circulation anomaly discussed above. This feature, along with the observed tropical anomaly, account for most of the stratospheric differences. The magnitudes of the observed and modeled TEM streamfunction are generally quite similar throughout the rest of the stratosphere. The model DJF TEM streamfunction compares very well with TEM

streamfunctions estimated by Rosenlof [1995] for January 1993 using computed radiative heating rates. The radiatively estimated TEM streamfunction does not show the circulation anomalies found in the UKMO analysis and instead shows a more gradual poleward and downward Brewer-Dobson circulation, similar to the LaRC IMPACT TEM streamfunction. The largest differences in the model and UARS-UKMO TEM streamfunction are confined to the troposphere, where interannual variability is higher than in the stratosphere (mostly due to the larger amplitude of the tropospheric TEM streamfunction). The modeled tropospheric streamfunction is uniformly larger in absolute amplitude than observed, indicating that the modeled DJF tropospheric Hadley circulation is stronger than is observed. The model stratospheric TEM streamfunction is generally within the expected interannual variability except near UARS-UKMO small scale circulation anomalies. The tropospheric differences are larger than would be expected due to interannual variability.

Figure 10 shows the JJA TEM streamfunction obtained from the UARS-UKMO assimilation and the model. The observed TEM streamfunction shows an unrealistic indirect tropospheric circulation (-) in NH middle latitudes, and an artifact of noise in the daily TEM streamfunctions in the upper stratosphere of the SH, but otherwise the patterns are nearly antisymmetric to their DJF counterparts. The differences in the JJA TEM streamfunction again reflect the stronger tropospheric Hadley circulation in the model.

The strength of the tropospheric Hadley circulation is largely determined by latent heat release within the tropical ITCZ. The overestimate of the tropospheric TEM circulation in the LaRC IMPACT model suggests that the model tropical latent heating may be too strong. Maximum estimated climatological DJF (JJA) diabatic heating rates of 0.8K/day (1.2K/day) occur at 300 hPa [Hoskins et al., 1989]. The model zonal mean tropical diabatic heating maxima (not shown) follow the seasonal migration of the ITCZ and reach peak amplitudes near 500 hPa of 1.2K/day in DJF and 1.4 K/day in JJA, somewhat lower in the troposphere and larger than observational estimates. As will be shown below, the IMPACT model has serious deficiencies in the representation of convective precipitation which is associated with the relatively low resolution spectral transport scheme. This leads to localized regions of excessive precipitation and release of latent heat. These latent heating anomalies are likely to contribute to the model's overestimate of the tropical diabatic heating. However, the differences noted here should be considered in light of the fact that heating rates are very difficult to determine reliably from assimilated data sets. Hoskins used the thermodynamic energy equation and ECMWF analyses to estimate diabatic

heating rates. Sardeshmukh [1993] has shown that this method can lead to underestimates in diabatic heating due to deficiencies in the ECMWF vertical velocities.

3.5) Geopotential Heights

One advantage of using a 3 dimensional model is the ability to simulate longitudinal asymmetries, particularly those associated with a distorted polar vortex. Geopotential heights (Z) provide a convenient measure of stratospheric vortex characteristics since they reflect the layer averaged temperatures and, geostrophically, indicate the strength of the polar night jet. The distribution of Z also provides an estimate of the model's ability to represent the horizontal and vertical structure of climatological planetary wave patterns.

Figure 11 shows polar stereographic plots of LaRC IMPACT, UARS-UKMO, and differences (UKMO-IMPACT) in seasonal mean Z at 500 hPa for years 2-5 of the simulation. Northern hemisphere DJF Z is in the left column and SH JJA Z is in the right column. The model reproduces the large-scale pattern of the observed NH 500 hPa DJF planetary wave pattern. The largest differences are associated with an amplified ridge over the North Atlantic, which is similar to observed blocking patterns, and a secondary ridge over the Pacific. The model tends to develop both Pacific and North Atlantic blocking patterns more frequently than is observed. Using the objective blocking definition of Tibaldi and Molteni [1990], we find that the frequency of North Atlantic blocks during DJF ranges from 45% to 65% in the model simulation, depending on which year is considered. The model DJF Pacific blocking patterns are highly variable from year to year, occurring 30% to 75% of the time. The observed frequency of blocking events are near 25% for North Atlantic and 20% for Pacific blocking patterns during DJF [Tibaldi and Molteni, 1990]. The difference pattern arising from the increased blocking frequency bears close resemblance to the observed North Atlantic Oscillation (NAO) [Wallace and Gutzler, 1981], and indicates that the model may be overestimating the negative phase of this fundamental mode of atmospheric interannual variability.

The sharp meridional gradients in geopotential height off the eastern coasts of North America and Asia in the observations and model reflect the climatological jet streams. The amplitudes of tropical and polar Z are consistent with observations indicating that the model layer mean

temperatures and equator to pole temperature gradients are reasonable. This agreement arises in spite of a DJF middle tropospheric cold bias of 5K because of the model's warm pole bias in the lower troposphere (see Figure 3). The modeled and observed 500 hPa SH Z fields are much more symmetric in JJA than their counterparts in the NH winter. Consequently, JJA differences between the model and UARS-UKMO climatology are largely zonally symmetric with the model showing a weaker vortex. The -20 dm difference in the center of the SH vortex results in a 20% reduction in meridional gradient in Z and accounts for the 5 ms^{-1} underestimate of the strength of the SH zonal winds between 50°S and 60°S in the low to mid troposphere (see Figure 2).

Figures 12, 13, and 14 show modeled and observed Z at 100 hPa, 10 hPa, and 1 hPa respectively. The model NH 100 hPa DJF Z shows a slight westward rotation of the trough over North America relative to climatology. The amplitude of the model NH 10 hPa DJF Aleutian high agrees with observations and results in a displacement of the vortex off the pole. However, the model Aleutian high is shifted west by nearly 45° compared to the UARS-UKMO climatology. The differences between the modeled and observed orientation of the NH 1 hPa DJF vortex arise due to the westward displacement of the Aleutian high at 1 hPa. The model vortex is also deeper than observed at 1 hPa. The model NH DJF differences from the UARS climatology at 100 hPa, 10 hPa, and 1 hPa all appear to be associated with the upward extension of the low geopotential height component (positive UKMO-IMPACT difference) of the 500 hPa Z over the North Atlantic associated with a higher frequency of North Atlantic blocking events in the model simulation. The difference pattern associated with this low geopotential height anomaly moves westward and poleward with altitude, resulting in a strengthening of the meridional gradient of Z near 60°N at 1 hPa compared to climatology. This is consistent with the poleward tilt of the model jet with altitude in the upper stratosphere during DJF.

The differences in the strength of the SH JJA vortex at 100 hPa and 10 hPa results in reductions in meridional gradient in Z at these altitudes similar to those found at 500 hPa. However, these weaker gradients are now associated with 15 ms^{-1} and 25 ms^{-1} underestimates in the zonal mean wind at 100 hPa and 10 hPa (see Figure 2). This occurs since zonal wind and geopotential height are related via the thermal wind relationship and weaker meridional gradients in Z introduce errors in zonal winds which increase with altitude. By 1 hPa this model bias has changed sign and the SH vortex is stronger in the model than the UARS-UKMO climatology.

Associated with this overestimate of the depth of the vortex at 1 hPa are a corresponding overestimate and poleward tilt of the SH JJA zonal mean westerlies (see Figure 2). However, unlike the NH case, we cannot attribute this upper stratospheric feature to any coherent planetary wave pattern originating in the troposphere.

3.6) Sea Level Pressure Anomalies

Synoptic-scale storms play a significant role in determining the tropospheric climatology through their meridional transport of heat, momentum and water vapor. Synoptic-scale storms are also often closely linked to stratospheric planetary wave events which are important in determining stratospheric variability. We use daily sea level pressure (SLP) anomalies to compare the characteristics of synoptic-scale storms in the model and UARS-UKMO climatology. Since the UARS UKMO data set does not include SLP we determine it hydrostatically from the 1000 hPa geopotential heights and temperatures. The derived monthly mean UKMO SLP distributions compare very well with NCEP monthly means.

Daily SLP anomalies are defined as the difference between the daily SLP and seasonal average SLP. The zonal mean is removed prior to determining the seasonal mean SLP (DJF and JJA) to remove the influence of secular changes in the zonal mean SLP. The zonal mean is also removed from the daily SLP. We focus on negative SLP anomalies since they are associated with storms. The mean amplitude of the negative SLP anomalies is a good indicator of the strength of tropospheric synoptic-scale storms. Figure 15 shows mean amplitudes of the UARS-UKMO and model negative SLP anomalies and differences (UKMO-IMPACT) for DJF and JJA. The observed mean amplitudes reach peaks of over 12 hPa in the NH winter and 10 hPa in the SH winter. The largest NH negative SLP anomalies are found within the climatological storm tracks off of the east coasts of North America and Asia during DJF. The largest SH negative SLP anomalies are found in the South Central Pacific during JJA. The UKMO summertime patterns are similar to their wintertime counterparts but the mean amplitudes are significantly lower in the NH, and somewhat lower in the SH.

The model DJF negative SLP anomalies have a structure which is similar to the UKMO climatology in the NH but the peak amplitude is smaller (6 hPa to 8 hPa) than observed, indicating a 4-6 hPa bias in the depth of synoptic scale storms in the North Atlantic. The model SH summertime (DJF) average amplitudes are slightly smaller than observed, extend further towards the

equator, and show largest amplitudes in the South Central Pacific. The model NH summer amplitudes are quite similar to the observed amplitudes except for a localized negative SLP anomaly over Newfoundland which is associated with an anomalous storm track pattern originating in the Gulf of Mexico.

A second measure of the quality of the model simulation of synoptic-scale storm dynamics is storm frequency. To determine storm frequency we count the number of days where the negative SLP anomalies are larger than 12 hPa for both the model and UKMO climatology. Figure 16 shows UARS-UKMO and model storm frequencies and differences (UKMO-IMPACT) for DJF and JJA. The patterns in Figure 16 are similar to those in Figure 15 since the negative SLP anomaly patterns are strongly influenced by the deepest anomalies. The observed wintertime storm frequencies peak at 20% in the NH storm tracks during DJF and in the SH South Central Pacific during JJA. The observed frequency of JJA storms is low in the NH and somewhat lower than the frequency of DJF storms in the SH. The model captures this seasonal variation in both NH and SH storm frequencies well, except the model SH JJA storm frequencies are 5-10% lower than observed. The largest differences are found during NH winter over the North Atlantic where the model underestimates the NH wintertime storm frequencies by 15%. This underestimate in NH wintertime storm frequencies is consistent with the increased frequency of North Atlantic blocking patterns discussed previously.

4) Tropospheric Radiative and Moisture Diagnostics

In this section we assess the quality of the model simulation of tropospheric radiative and moist processes by comparing the distributions of outgoing longwave radiation (OLR), precipitation, precipitable water, and cloudiness in the model to observed climatologies. Plate 2 shows the zonal mean annual distributions of OLR, precipitation, precipitable water, and total cloudiness for the model for each year of the 5 year simulation along with observed climatologies. The OLR climatology was obtained from the Earth Radiation Budget Experiment (ERBE) [Barkstrom, 1984] during the period from 1985 to 1989. The observed precipitation climatology is from Version 1a of the Combined Precipitation data set compiled by the Global Precipitation Climatology Project (GPCP) [Huffman, 1997] for the period from 1987 to 1996. Precipitable water and total cloudiness estimates are from the International Satellite Cloud Climatology Project (ISCCP) [Rossow, 1991] for the period from 1984 through 1990, excluding 1985. The observed zonal mean annual

distributions were obtained by averaging monthly mean global data sets.

The model zonal mean annual OLR compares quite well with observations in the tropics but significantly underestimates the middle latitude annual OLR where differences between the model and ERBE OLR are on the order of 15 Wm^{-2} . The model annual average precipitation is comparable to GPCP estimates in the tropics, but the model tropical peak is significantly broader than observed. The model midlatitude precipitation is significantly larger than observed. The excess subtropical precipitation is associated with overestimates of the large-scale precipitation over oceans (typically within the lowest level of the model) while the excess mid-latitude precipitation is primarily due to overestimates of convective precipitation over land. The large errors in the annual mean distribution of middle latitude precipitation are believed to be due to our relatively primitive convective precipitation parameterization and indicate serious problems with the model hydrological cycle. However, in spite of the problems with the model's representation of precipitation processes, the model zonal mean annual precipitable water distribution compares quite well with ISCCP observations. The major model deficiency is a 10% underestimate of tropical annual mean precipitable water. The amount and distribution of precipitable water in the model is determined by a balance between water vapor sinks (precipitation), water vapor sources (surface latent heat flux) and water vapor transport. The fact that the model midlatitude precipitable water is in good agreement with observations in spite of the significant excesses in mid-latitude precipitation suggests that the model overestimates surface latent heat flux and/or transports more water vapor out of the tropics than is observed. Excessive latent heat flux over the warm tropical oceans is consistent with excess low level subtropical precipitation, while the underestimate of the tropical precipitable water suggests the poleward water vapor transport may be too strong in the model.

The model zonal mean annual cloud frequencies are in good agreement with the ISCCP climatology in the tropics and subtropics. The model captures the main meridional features of the observed total cloudiness in these latitudes including the tropical maximum (associated with high convective clouds) and subtropical minima (associated with the descending branches of the tropical Walker cell). The SH middle latitude cloudiness is underestimated in the model while polar cloud frequencies are significantly larger than observed. However, the low ISCCP cloud frequencies in polar latitudes could be due to problems in distinguishing between cold, snow covered surfaces and clouds in the satellite retrievals. The LaRC IMPACT model cloud frequencies are

very similar to the Max Planck Institute for Meteorology ECHAM4 GCM cloud frequencies [Chen and Roeckner, 1997]. Chen and Roeckner show that ISCCP polar cloud frequencies are consistently underestimated relative to both the ECHAM4 model and ground based observations.

The distribution of OLR serves as a good overall estimate of the consistency of the simulation of tropospheric radiative and moist processes since it is sensitive to the mean tropospheric temperature, column water vapor, and the distribution of high clouds. The agreement between the model OLR and ERBE climatology in the deep tropics is due to the good characterization of the zonal mean annual distribution of high, cold convective clouds in the model, which act to reduce the tropical OLR. The agreement in the model and ERBE subtropical OLR maxima arises in spite of the underestimate of total column water vapor at these latitudes because the model mid-tropospheric cold bias reduces the upwelling longwave fluxes. The reduced upwelling longwave fluxes compensate for the underestimates in tropical water vapor longwave absorption. On the other hand, the model precipitable water is in good agreement with climatology in middle latitudes, so that the model mid-tropospheric cold bias results in an underestimate in midlatitude OLR.

Figures 17 through 20 show DJF and JJA comparisons of the global distribution of observed OLR, precipitation, precipitable water, and total cloudiness with the model years 2-5 of the simulation. Differences (observed-IMPACT) are also shown. The model OLR (Fig. 17) captures the large-scale patterns and extrema of the observed DJF OLR. High OLR ($> 265 \text{ Wm}^{-2}$ is shaded) is found over the subtropical oceans and the African Sahara. Lowest OLR ($155\text{-}175 \text{ Wm}^{-2}$) is found over the ice-covered continents of Greenland and Antarctica. The narrow bands of low tropical OLR extending eastward from South America and Southern Africa are due to high cloudiness (see Fig. 20) and high precipitable water (see Fig. 19) within the ITCZ. The largest OLR differences are negative (model overestimates OLR) and are found over Brazil (-80 Wm^{-2}) and South Africa (-40 Wm^{-2}). These overestimates in OLR are due to underestimates in precipitable water in these regions (see Fig. 19). Convective cloudiness over South America and Southern Africa is displaced southward in the model (see Fig. 20) resulting in 40 to 60 Wm^{-2} positive differences south of the observed convective regions. Elsewhere, the DJF OLR differences are generally less than 20 Wm^{-2} . The model reproduces the patterns and magnitudes of the observed OLR during JJA except over western North America and within the Asian Summer Monsoon region, where the model shows a pattern of small-scale maxima and minima. This small-scale pat-

tern in model OLR is closely linked to the pattern of high precipitation (see Fig. 18) and high cloud frequency (see Fig. 20), particularly in the Asian Summer Monsoon region.

The model precipitation distribution (Fig. 18) is significantly different than observed. The precipitation field is dominated by localized regions of excessive precipitation ($> 6\text{mm/day}$ are shaded) which account for most of the differences between the model and GPCP observations. Particularly large differences are found north of the Mediterranean Sea in DJF and over the Tibetan Plateau during JJA. Examination of daily precipitation distributions shows that these excessive precipitation events occur at only a few grid points and tend to be orographically locked. The degree of small-scale structure in the model precipitation distribution, particularly over the NH land masses, indicates that orographically locked grid point rain events are leading to “spectral rain” in the model simulation. Spectral rain is a numerical artifact which frequently occurs in models which use spectral water vapor transport and arises due to inadequate spectral representation of localized maxima in the model water vapor distribution. These local maxima tend to develop as a result of strong vertical advection of water vapor in response to localized convective latent heat release. However, in spite of these severe limitations, some realistic features can be seen in the model precipitation distribution. The model shows enhanced precipitation within mid-latitude storm tracks off the east coasts of the North American and Asian continents during DJF and also in SH mid-latitudes during JJA, which agree with observations. The model shows enhanced precipitation within the ITCZ during DJF but the precipitation pattern is broader and weaker than is observed, particularly in the equatorial western Pacific. The model fails to capture the oceanic precipitation within the ITCZ during JJA. The model minimum precipitation exceeds 2 mm/day over most of the tropical and mid-latitude oceans while the GPCP estimates indicate that precipitation is virtually absent in the subtropical high pressure systems found to the west of South America and South Africa.

The modeled distribution of precipitable water (Fig. 19) is reasonable during both DJF and JJA. The highest precipitable water ($> 40\text{kgm}^{-2}$ is shaded) is found within the ITCZ during both seasons and in the South Pacific Convergence Zone during DJF. The model precipitable water is generally within 5 kgm^{-2} of the observed climatology except for over South America and the western coasts of South America and South Africa, where the model underestimates the amount of precipitable water by $15\text{-}20\text{ kgm}^{-2}$. As discussed above, the low model precipitable water is

consistent with the overestimate of OLR in these regions (see Fig. 17). The western coasts of continents are regions of persistent marine boundary layer clouds. The model PBL is not able to adequately represent the turbulent flux of latent heat responsible for the development of the low level cumulus associated with the trade inversion, and consequently underestimates the amount of precipitable water found in these regions. The model precipitable water is within 5 kgm^{-2} of the ISCCP climatology over the North American and Asian continents during both DJF and JJA except near the Tibetan Plateau. The large positive difference south of the Tibetan Plateau during JJA is due to the sharp meridional gradient in precipitable water associated with orographic blocking in the ISCCP data set which is not captured by the model due to the relatively smooth representation of orography in the model. The model tends to overestimate the poleward transport of water vapor from the tropical source regions into the NH, leading to $5\text{-}10 \text{ kgm}^{-2}$ overestimates of the amount of precipitable water over NH oceans. The underestimate of precipitable water off of the western coast of North America during JJA is due to the lack of realistic marine boundary layer latent heat fluxes and cloud formation in this region, similar to the SH deficits discussed earlier.

The model total cloud frequencies (Fig. 20) capture the main features of the observed total cloud frequency over land during both DJF and JJA. These features include the persistent low cloudiness (values $< 40\%$ are shaded) over the African Sahara and Australia, the high cloud frequency over Brazil and South Africa during DJF, and then migration of the high cloud frequency patterns northward during JJA. Cloudiness is overestimated by 20% over North America and much of Asia during DJF. The persistent high cloudiness observed within the northern and southern hemisphere storm tracks is underestimated by 20% in the model, particularly during JJA in the NH, where the storm track cloud signature is absent in the model. The persistent low cloudiness over Greenland and Antarctica in the ISCCP climatology leads to large apparent overestimates of model cloudiness in these regions but is likely due to underestimates of clouds over snow and ice in the ISCCP climatology and does not necessarily imply model deficiencies. The low model cloud frequencies to the west of North America, South America, and Southern Africa are due to the lack of realistic marine boundary layer clouds, as discussed earlier.

5) Summary and conclusions

The LaRC IMPACT model winds and temperatures are in good agreement with UARS-UKMO assimilated winds and temperatures in the lower stratosphere. Accurate prediction of lower stratosphere winter vortex temperatures is particularly important for successful simulations with a coupled middle atmosphere model since parameterizations of heterogeneous chemistry on polar stratospheric clouds are highly temperature dependent. Minor systematic changes in mid-winter vortex temperatures, either warmer or colder, can result in significantly different spring-time ozone photochemistry in both the northern and southern hemispheres due to denitrification and release of active chlorine when sunlight returns to the pole. The model tropopause is consistently 5-10K colder than climatology. The tropopause cold bias could adversely impact lower stratospheric heterogeneous processing on cold sulfate aerosols under heavy aerosol loading. The model upper stratospheric zonal mean temperatures agree with the UARS-UKMO climatology except for the winter cold pole which results from the upward extension of the cold vortex temperatures and an elevated winter stratopause in the model. The cold bias is consistent with the overprediction of the winter stratospheric jet strength. This “cold pole” bias is a characteristic of stratospheric GCMs in general. In fact, Butchart and Austin [1998] compared an 11 year climatology of the UKMO Unified Model (which is used in the UARS-UKMO assimilation) and the UARS-UKMO climatology and found wind and temperature biases similar to those reported here. The LaRC IMPACT model stratopause temperatures compare better with observationally based upper stratosphere climatologies than the UARS-UKMO assimilated temperatures do.

The model NH and SH stratospheric eddy heat and momentum fluxes are within the expected interannual variability of the UARS-UKMO climatology. The poleward displacement of the DJF stratospheric eddy momentum flux is consistent with the poleward tilt of the model DJF zonal mean westerlies. The model tropospheric heat and momentum fluxes capture the main features of the observed climatology, indicating an adequate treatment of mid-latitude moist baroclinic development, although the model has somewhat weaker eddy momentum flux near the tropospheric jet cores and underestimates the magnitude of the eddy heat fluxes at the middle latitude tropopause. This discrepancy is most likely related to the relatively coarse vertical resolution at the model tropopause. DJF 500 hPa height patterns are in good agreement with the UARS-UKMO climatology except for the North Atlantic, where blocking patterns are more frequent than are observed. The increased frequency of North Atlantic blocking leads to systematic stratospheric geopotential height differences between the model and UARS-UKMO climatology asso-

ciated with the westward displacement of the Aleutian High. The differences associated with this height anomaly propagate upward and poleward and contribute to a strengthening of the 1hPa geopotential height gradient at 60°N. The stronger height gradient contributes to the poleward tilt of the NH stratospheric DJF jet in the model.

The inclusion of water vapor transport and parameterizations of physical processes in the model troposphere is a major advancement in the development of the coupled LaRC IMPACT model. The combined effects of water vapor transport, radiative, convective, and planetary boundary layer parameterizations have been shown to produce tropospheric temperatures, winds, and circulation statistics that are in relatively good agreement with the UARS-UKMO climatology although the model upper tropospheric temperatures are ~5K too cold. The model simulates the distribution and life-cycle of wintertime synoptic-scale storms reasonably well, suggesting that a primary source of stratospheric planetary wave variability, namely transient tropospheric eddies, is adequately represented. Comparisons between the model and UARS-UKMO climatology indicates that the model does a reasonable job in reproducing the frequency of observed synoptic-scale storms during the northern and southern hemisphere winters. The model shows enhanced storm activity off of the eastern coasts of North America and Asia during DJF and in the South Central Pacific during JJA, in good agreement with the UKMO climatology, but the model underestimates the mean amplitude and frequency of the North Atlantic winter storms due to the persistent blocking patterns in the model simulation. The model overestimates the meridional extent and frequency (but not the amplitude) of summertime storm activity in the South Central Pacific, but this is a region of large interannual variability in storm frequency in the UARS UKMO climatology, so the differences between observations and the model are less significant.

Investigation of lower stratosphere/upper troposphere chemistry requires that tropospheric thermal structure and mean circulation patterns are well represented and that the large-scale distribution of tropical convective systems is adequate since much of the tropical stratosphere/troposphere exchange occurs in conjunction with deep convection over maritime continents. The generally good agreement between the model and observations of the distributions of OLR and precipitable water, as well as hemispheric budgets of these quantities, indicates that the T32 spectral resolution is adequate for determining the large-scale transport of heat and water vapor within the free troposphere. However, the presence of spectral signatures in the distribution of precipitation indicates that the T32 spectral resolution of the model is probably not adequate to accurately

represent coupling between localized convection and large-scale water vapor transport, resulting in significant errors in the model precipitation. This inadequacy is manifested in a poor simulation of convective precipitation and associated cloudiness in the JJA Asian Monsoon, which leads to the small-scale patterns in OLR and cloud frequency in this region.

An accurate representation of the time-averaged meridional circulation is critical to long-term stratospheric coupled chemistry and dynamics simulations since the photochemical evolution of the stratosphere is largely determined by the distributions of source gases, which are strongly influenced by the mean circulation. The TEM circulation reflects the balance between seasonal temperature changes and time-averaged diabatic heating rates (through the TEM thermodynamic energy equation) and the balance between Eliassen-Palm flux divergence and parameterized momentum sinks (through the TEM momentum equation) [Andrews et al., 1987]. Consequently, it is a good overall measure of the integrity of the dynamical response to the model's diabatic heating, frictional, and gravity-wave parameterizations. The model stratospheric radiative calculations are directly influenced by the modeled ozone distributions so that the TEM circulation also reflects the stratospheric response to radiative/photochemical coupling. The overall good agreement between the observed and modeled stratospheric TEM circulations and the stability of the model climatology provides confidence that the LaRC IMPACT model is appropriate for multi-year coupled radiation/chemistry/dynamics studies of the stratosphere.

Figure Captions:

Figure 1: Model DJF zonal mean winds (m/s) for years 2-5 of the simulation compared with the UARS-UKMO climatology. The upper left panel shows the UARS-UKMO climatological zonal mean winds, the upper right panel shows the LaRC IMPACT model winds, the lower left panel shows the standard deviation of the DJF zonal winds indicating the amount of interannual variability expected. The lower right panel shows the differences between the UKMO and LaRC zonal winds. Shaded regions indicate where these differences are larger than 4 standard deviations from the UKMO climatology and are therefore outside the expected interannual variability.

Figure 2: Same as Figure 1 for JJA zonal mean winds.

Figure 3: Same as Figure 1 for DJF zonal mean temperatures (K).

Figure 4: Same as Figure 1 for JJA zonal mean temperatures (K).

Figure 5: Same as Figure 1 for DJF total eddy momentum fluxes ($\overline{u'v'}$) in m^2s^{-2} .

Figure 6: Same as Figure 1 for JJA total eddy momentum fluxes ($\overline{u'v'}$) in m^2s^{-2} .

Figure 7: Same as Figure 1 for DJF total eddy heat fluxes ($\overline{v't'}$) in ms^{-1}K .

Figure 8: Same as Figure 1 for JJA total eddy heat fluxes ($\overline{v't'}$) in ms^{-1}K .

Figure 9: Same as Figure 1 for DJF TEM streamfunction ($\text{Kgm}^{-1}\text{s}^{-1}$).

Figure 10: Same as Figure 1 for JJA TEM streamfunction ($\text{Kgm}^{-1}\text{s}^{-1}$).

Figure 11: Polar stereographic plots of UARS-UKMO (upper), model (middle) and differences (UKMO-IMPACT, lower) Geopotential height, Z, (dm) at 500 hPa for years 2-5 of the simulation. Northern hemisphere DJF Z is in the left column and SH JJA Z is in the right column.

Figure 12: Same as Figure 11 for 100 hPa

Figure 13: Same as Figure 11 for 10 hPa

Figure 14: Same as Figure 11 for 1 hPa

Figure 15: Mean amplitudes of the UARS-UKMO and model negative SLP anomalies (hPa) and differences (UKMO-IMPACT) for DJF and JJA. Regions with mean anomalies with amplitudes greater than 8hPa are shaded.

Figure 16: UARS-UKMO and model storm frequencies (%) and differences (UKMO-IMPACT) for DJF and JJA. Regions with storm frequencies greater than 10% are shaded.

Figure 17: Global distribution of ERBE observed (upper), model (middle) and difference (observed- model) OLR (Wm^{-2}) for DJF (left panels) and JJA (right panels). Regions with OLR greater than 265 Wm^{-2} are shaded.

Figure 18: Global distribution of GPCP observed (upper), model (middle) and difference (observed- model) precipitation (mmday^{-1}) for DJF (left panels) and JJA (right panels). Regions with precipitation greater than 6 mmday^{-1} are shaded.

Figure 19: Global distribution of ISCCP observed (upper), model (middle) and difference

(observed- model) precipitable water (kgm^{-2}) for DJF (left panels) and JJA (right panels). Regions with precipitable water greater than 40 kgm^{-2} are shaded.

Figure 20: Global distribution of ISCCP observed (upper), model (middle) and difference (observed- model) total cloud fraction (%) for DJF (left panels) and JJA (right panels). Regions with total cloud fractions less than 60% are shaded.

Plate Captions

Plate 1: Timeseries of northern and southern hemisphere 10 hPa polar temperatures, zonal mean winds, and wave number 1 and 2 geopotential heights, for each of the five years of the model simulation and UKMO observations.

Plate 2: Zonal mean annual distributions of OLR, precipitation, precipitable water, and total cloudiness for the model for each year of the 5 year simulation along with observed ERBE, GPCP, and ISCCP climatologies.

References:

- Anderson, W. K., J. L. Thomas, and B. Van Leer, Comparison of Finite Volume Flux Vector Splittings for the Euler Equations, *AIAA Journal*, 24, 1453-1460, 1986.
- Andrews, D. G., J. R. Holton, and C. B. Leavy, *Middle Atmosphere Dynamics*, 489pp., Academic, San Diego, Ca, 1987.
- Barkstrom, B. R., The Earth Radiation Budget Experiment (ERBE), 1984: *Bull Am. Meteorol. Soc.*, 65, 1170-1185.
- Barnett, J. J. and M. Corney, *Handbook for Middle Atmosphere Program (MAP)*, SCOSTEP Secretariat, University of Illinois, Urbana, Illinois, USA, 61801, 16, 47, 1985.
- Beagley, S. R. , J. de Grandpre, J. N. Koshyk, N. A. McFarlane, and T. G. Shepherd, Radiative-Dynamical Climatology of the First-Generation Canadian Middle Atmosphere Model, *Atmos-Ocean*, 35 293-331, 1997.
- Blackshear, W.T., W.L. Grose, and R.E. Turner, Simulated sudden stratospheric warming, *Synop-*

- tic evolution, Q. J. R. Meteorol. Soc., 113, 815-846, 1987.
- Boville, B. A., Middle atmosphere version of CCM2 (MACCM2): Annual cycle and interannual variability, J. Geophys. Res., 100, 9017-9039, 1995.
- Butchart, N. and J. Austin, Middle Atmosphere Climatologies from the Troposphere-Stratosphere Configuration of the UKMO's Unified Model, J. Atmos. Sci., 55, 2782-2809, 1998.
- Chandra, S. E. L. Fleming, M. R. Schoeberl, and J. J. Barnett, Monthly mean global climatology of temperature, wind, geopotential height and pressure for 0-120 km, Adv. Space Res., 10, (6)3-(6)12, 1990.
- Chen, C.-T., and E. Roeckner, Cloud simulations with the Max Planck Institute for Meteorology general circulation model ECHAM4 and comparison with observations, J. Geophys. Res., 102, 9335-9350, 1997.
- Coy, L. and R. Swinbank, Characteristics of stratospheric winds and temperatures produced by data assimilation, J. Geophys. Res., 102, 25,763-25,781, 1997.
- Cullen, M. J. P., The unified forecast/climate model, Meteorol. Mag., 122, 81-94, 1993.
- Eckman, R. S., W. L. Grose, R. E. Turner, W. T. Blackshear, J. M. Russell III, L. Froidevaux, J. W. Waters, J. B. Kumer, A. E. Roche, Stratospheric trace constituents simulated by a three-dimensional general circulation model, J. Geophys. Res., 100, 13951-13966, 1995.
- Eckman, R. S., W. L. Grose, R. E. Turner, and W. T. Blackshear, Polar ozone depletion: A three-dimensional chemical modeling study of its long-term global impact, J. Geophys. Res., 101, 22,977-22,989, 1996.
- Eliassen, E., B. Machenaur, and E. Rasmussen, On a numerical method for integration of the hydrodynamic equations with a spectral representation of the horizontal fields, Inst. of Theor. Met., Univ. of Copenhagen, Report No. 2, 1970.
- Farman, J. C., B. G. Gardiner, and J. D. Shanklin, Large losses of ozone in Antarctica reveal seasonal ClO_x/NO_x interaction, Nature, 315, 207-210, 1985.
- Grose, W. L. Recent advances in understanding stratospheric dynamics and transport processes: Application of satellite data to their interpretation, Adv. Space Res., 4, 19-28, 1984.
- Grose, W. L., J. E. Nealy, R. E. Turner, and W. T. Blackshear, Modeling the transport of chemically active constituents in the stratosphere, in *Transport Processes in the Middle Atmosphere*, pp. 229-250, edited by T. Scheider et al., D. Reidel, Norwell, Ma, 1987
- Hamilton, K., R. J. Wilson, J. D. Mahlman, and L. J. Umscheid, Climatology of the SKYHI Tro-

- posphere-Stratosphere-Mesosphere General Circulation Model, *J. Atmos. Sci.*, 52, 5-43, 1995.
- Haynes, P. H., C. J. Marks, M. E. McIntyre, T. G. Shepherd, and K. P. Shine, On the “Downward Control” of Extratropical Diabatic Circulations by Eddy-Induced Mean Zonal Forces, *J. Atmos. Sci.*, 48, 651-678, 1991.
- Holton, J. R., A Semi-Spectral Numerical Model for Wave-Mean Flow Interactions in the Stratosphere: Application to Sudden Stratospheric Warmings, *J. Atmos. Sci.*, 1639-1649, 1976.
- Hoskins, B.J., and A.J. Simmons, A multilayer model and the semi-implicit method. *Q. J. R. Meteorol. Soc.*, 101, 637-655, 1975.
- Hoskins, B. J., H. H. Hsu, I. N. James, M. Masutani, P. D. Sardeshmukh, and G. H. White, Diagnostics of the global atmospheric circulation: Based on ECMWF analyses 1979-1989. World Climate Programme, World Meteorological Organization Report No. 326, 217pp., 1989.
- Huffman, ed., 1997: The Global Precipitation Climatology Project monthly mean precipitation data set. WMO/TD No. 808, WMO, Geneva, Switzerland. 37pp.
- Johnson, D. R., The forcing and maintenance of global monsoonal circulations: An isentropic analysis. *Advances in Geophysics*, Vol. 31, Academic, 1989.
- Press, 43-316. Kalnay, E., R. Balgovind, W. Chao, D. Edlmann, J. Pfaendtner, L. Takacs, and K. Takano, NASA Tech. Mem. 86064, NASA Goddard Space Flight Center, Greenbelt, MD 20771, 1983
- Kessler, E., On the distribution and continuity of water substance in atmospheric circulations, *Meteor. Monogr.*, 32, Amer. Meteor. Soc., 84pp., 1969.
- Kuo, H.L., Further Studies of the Parameterization of the Influence of Cumulus Convection on Large-Scale Flow, *J. Atmos. Sci.*, 31, 1232-1240, 1974.
- McFarlane, N.A., McFarlane, N.A., The effect of orographically excited gravity-wave drag on the circulation of the lower stratosphere and troposphere. *J. Atmos. Sci.*, Vol. 44, No 14, 1775-1800, 1987.
- Molinari, J., A Method for Calculating the Effects of Deep Cumulus Convection in Numerical Models, *Mon. Wea. Rev.*, 110, 1527-1534, 1982.
- Orszag, S. A., Transform method for calculation of vector coupled sums: application to the spectral form of the vorticity equation, *J. Atmos. Sci.*, 27, 890-895, 1970.
- Pawson, S. et al., The GCM-Reality Intercomparison Project for SPARC (GRIPS): Scientific Issues and Initial Results, Accepted to *Bull. Am. Meteorol. Soc.*, March, 2000.

- Phillips, N.A., A coordinate system having some special advantages for numerical forecasting, *J. Meteor.*, 14, 184-185, 1957.
- Pierce, R.B., W.T. Blackshear, T.D. Fairlie, W.L. Grose, R.E. Turner, The interaction of radiative and dynamical processes during a simulated sudden stratospheric warming, *J. Atmos. Sci.*, 50, 3829-3851, 1993
- Rind, D., R. Suozzo, N. K. Balachandran, A. Lacis, and G. Russell, The GISS Global Climate-Middle Atmosphere Model. Part I: Model Structure and Climatology, *J. Atmos. Sci.* 45, 329-370, 1988.
- Robert, A.J., J. Henderson, and C. Turnbull, An implicit time integration scheme for baroclinic modes of the atmosphere, *Mon. Wea. Rev.*, 100, 329-335, 1972.
- Rosenlof, K. H., Seasonal cycle of the residual mean meridional circulation in the stratosphere, *J. Geophys. Res.*, 100, 5173-5191, 1995.
- Rossow, W.B., L.C. Garder, P.J. Lu, and A.W. Walker, 1991: International Satellite Cloud Climatology Project (ISCCP) Documentation of Cloud Data. WMO/TD-No. 266, World Meteorological Organization, 76 pp. plus appendices.
- Sardeshmukh, P. D., The Baroclinic χ Problem and its application to the diagnosis of atmospheric heating rates, *J. Atmos. Sci.*, 50, 1099-1112, 1993.
- Shepherd, T. G., K. Semeniuk, and J. N. Koshyk, Sponge layer feedbacks in middle-atmosphere models, *J. Geophys. Res.*, 101, 23,447-23,464, 1996.
- Shine, K.P., The middle atmosphere in the absence of dynamical heat fluxes, *Q.J.R. Meteorol. Soc.*, 113, 605-633, 1987
- Stolarski, R. S. P. Bloomfield, R. D. McPeters, and J. R. Herman, Total Ozone Trends Deduced from NIMBUS 7 TOMS Data, *Geophys. Res. Lett.*, 18, 1015-1018, 1991.
- Swinbank, R., and A. O'Neill, A Stratosphere-Troposphere Data Assimilation System, *Mon. Wea. Rev.*, 122, 686-702, 1994.
- Tibaldi, S. and F. Molteni, On the operational predictability of blocking, *Tellus*, 42A, 343-365, 1990.
- Wallace, J. M., and D. S. Gutzler, Teleconnections in the Geopotential Height Field during The Northern Hemisphere Winter, *Mon. Wea. Rev.*, 109, 784-812, 1981.
- Williamson, D. L., J. T. Kiehl, V. Ramanathan, R. E. Dickinson, and J. J. Hack, Description of the NCAR Community Climate model (CCM1), NCAR Technical Note 285, Boulder, Colo.,

1987.

Zapotocny, T.H., D.R. Johnson, F.M. Reames, R.B. Pierce, and B.J. Wolf, Numerical Investigations with a Hybrid Isentropic-Sigma Model. Part II: The Inclusion of Moist Processes. J. Atmos. Sci., Vol. 48, No. 18, 2025-2043, 1991.

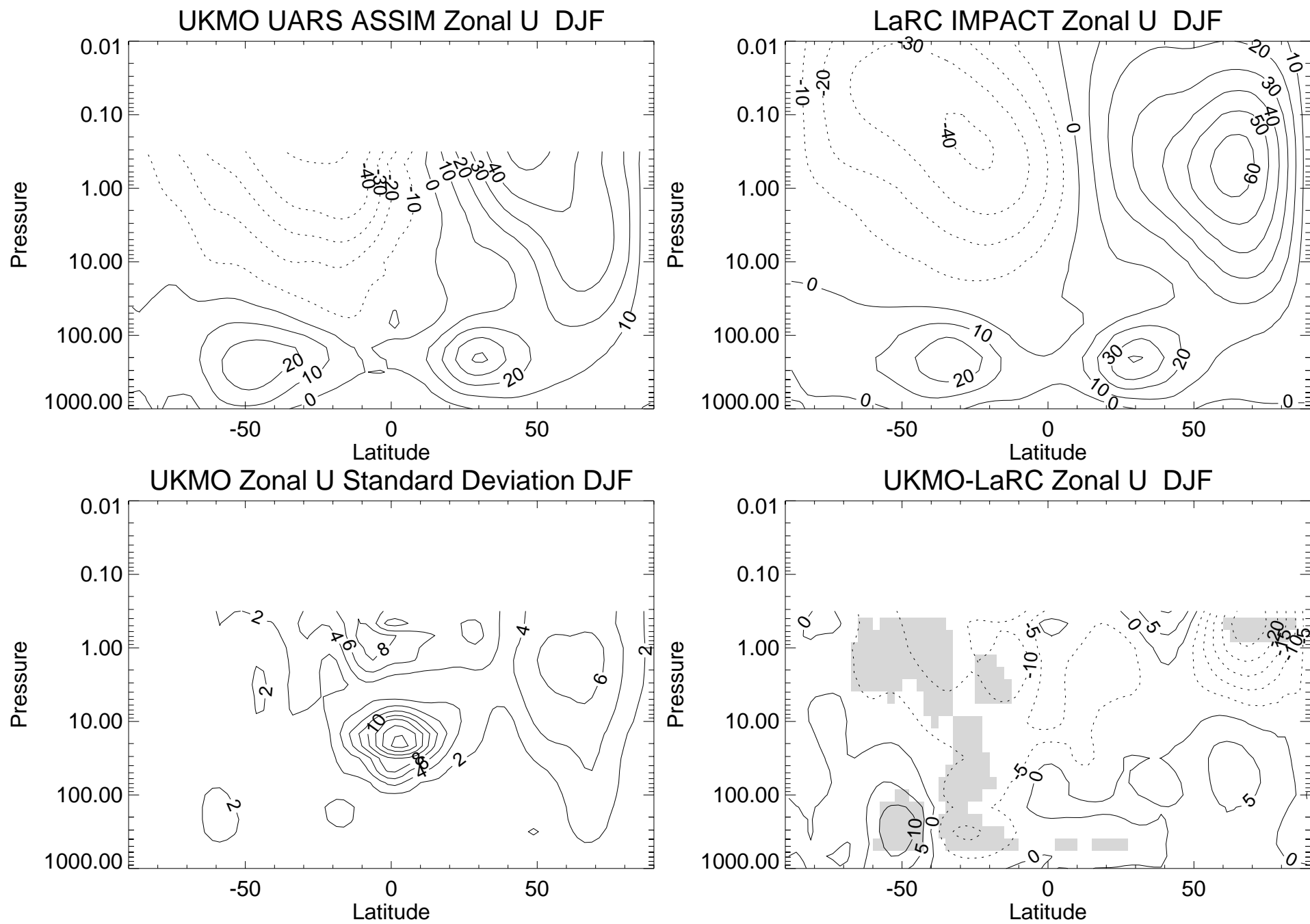


Figure 1

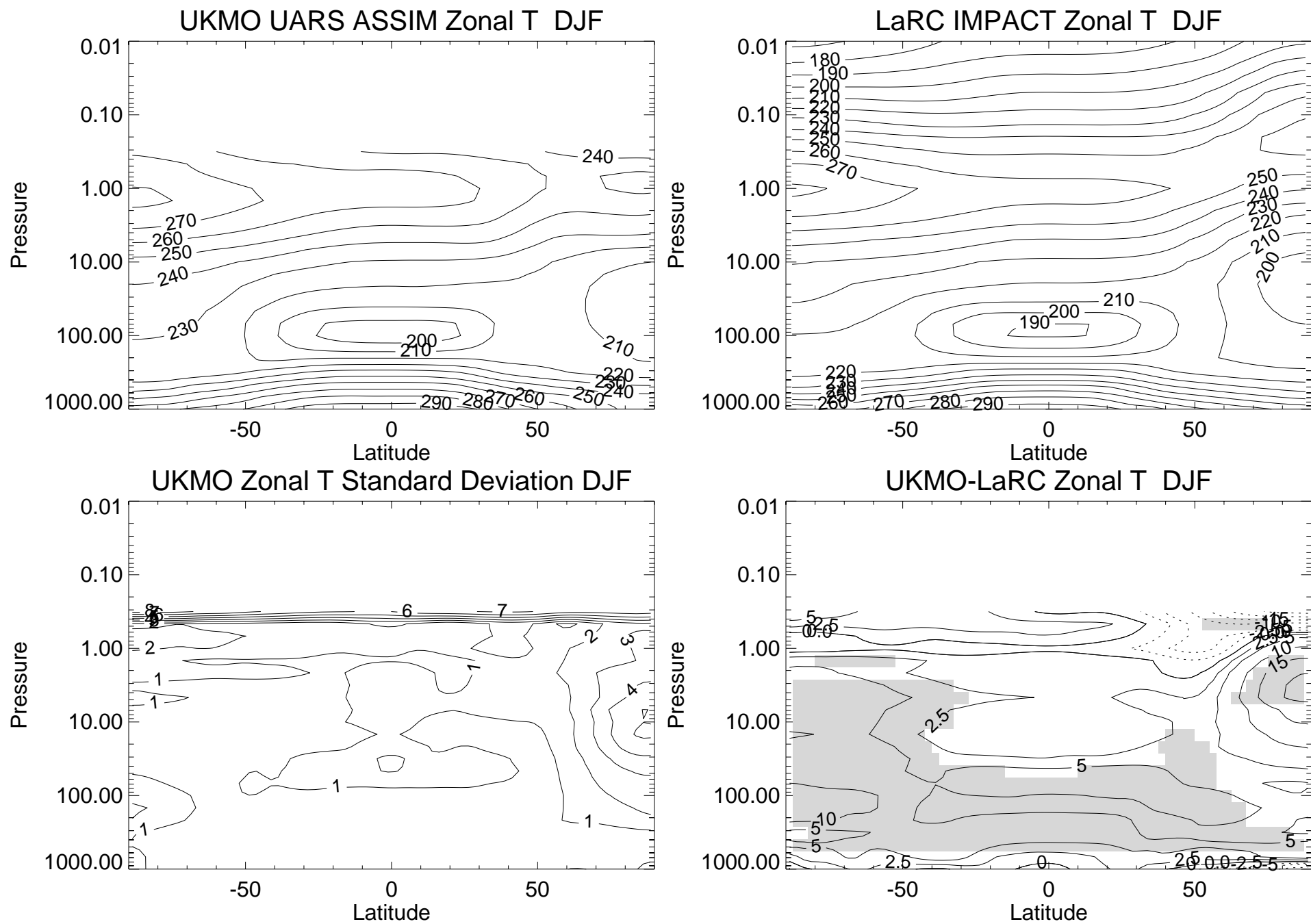


Figure 2

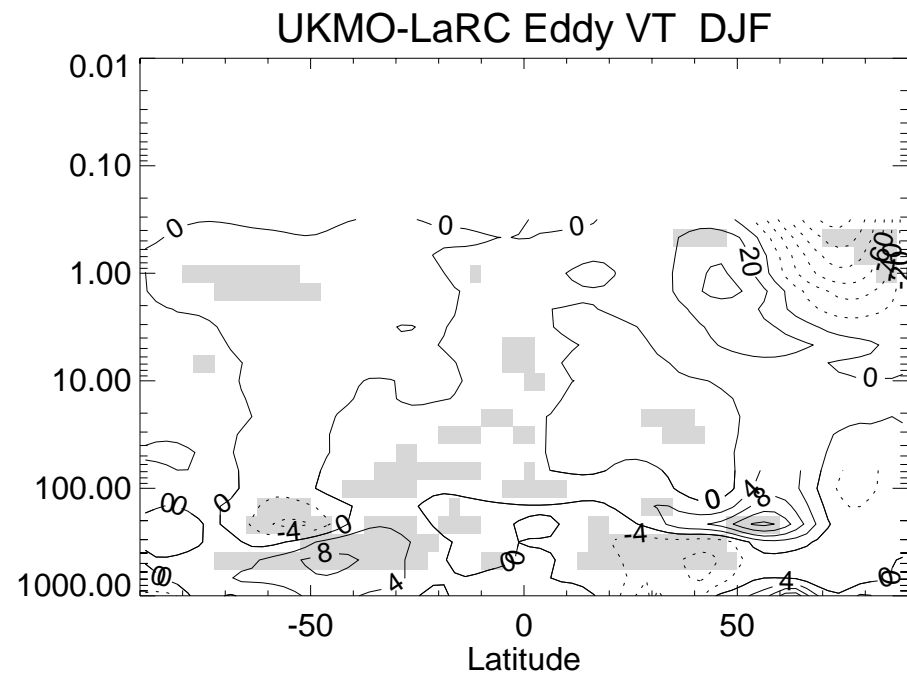
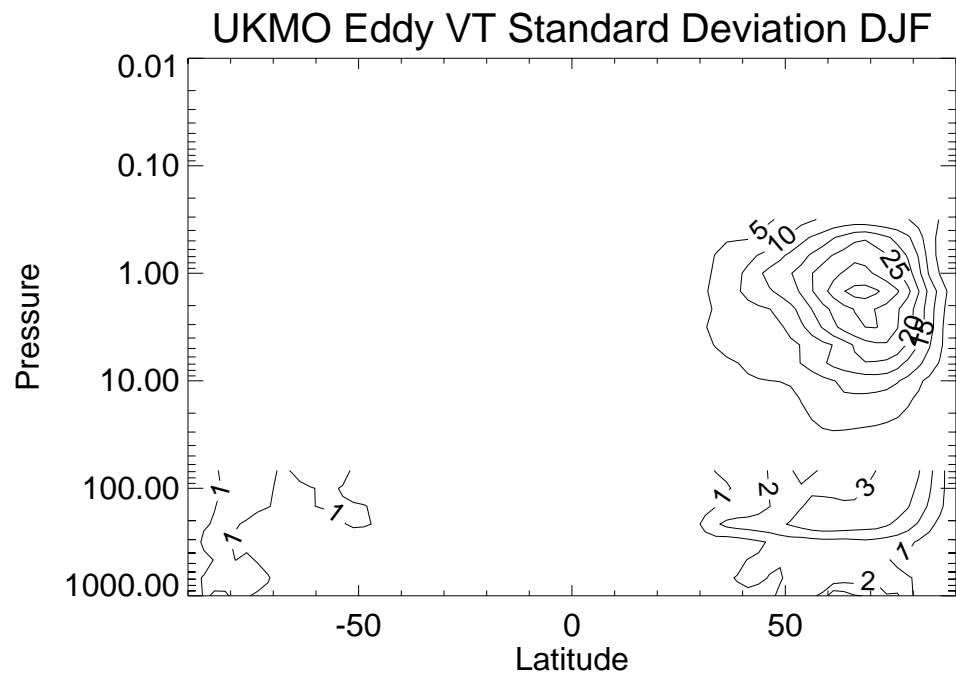
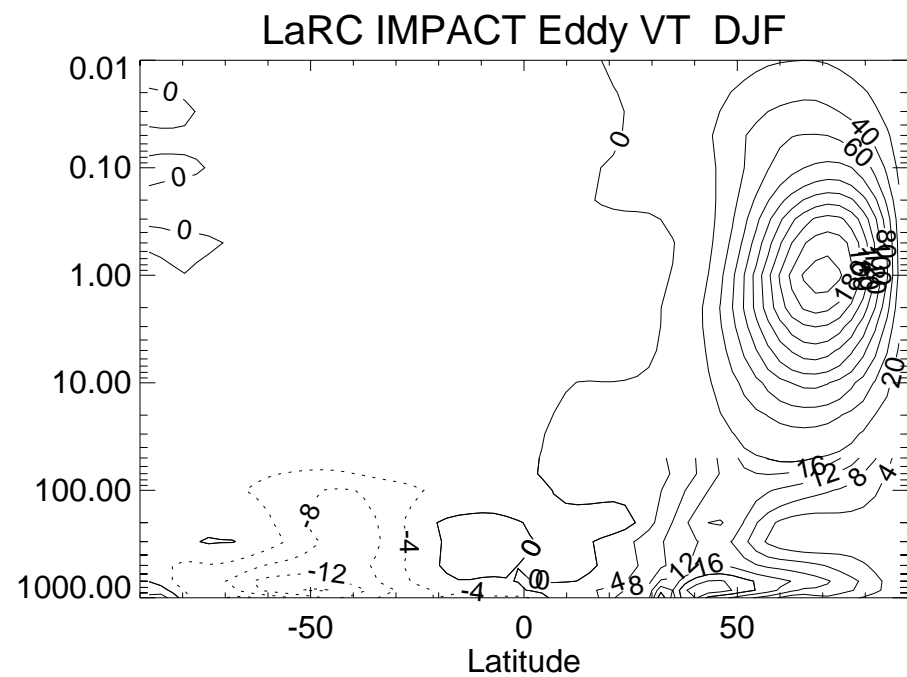
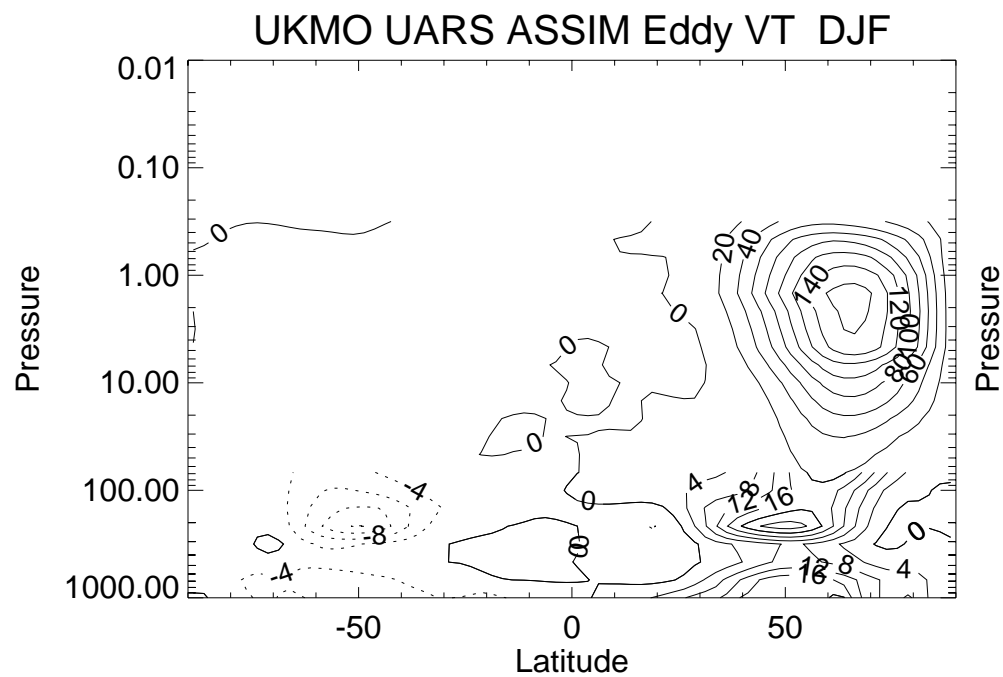
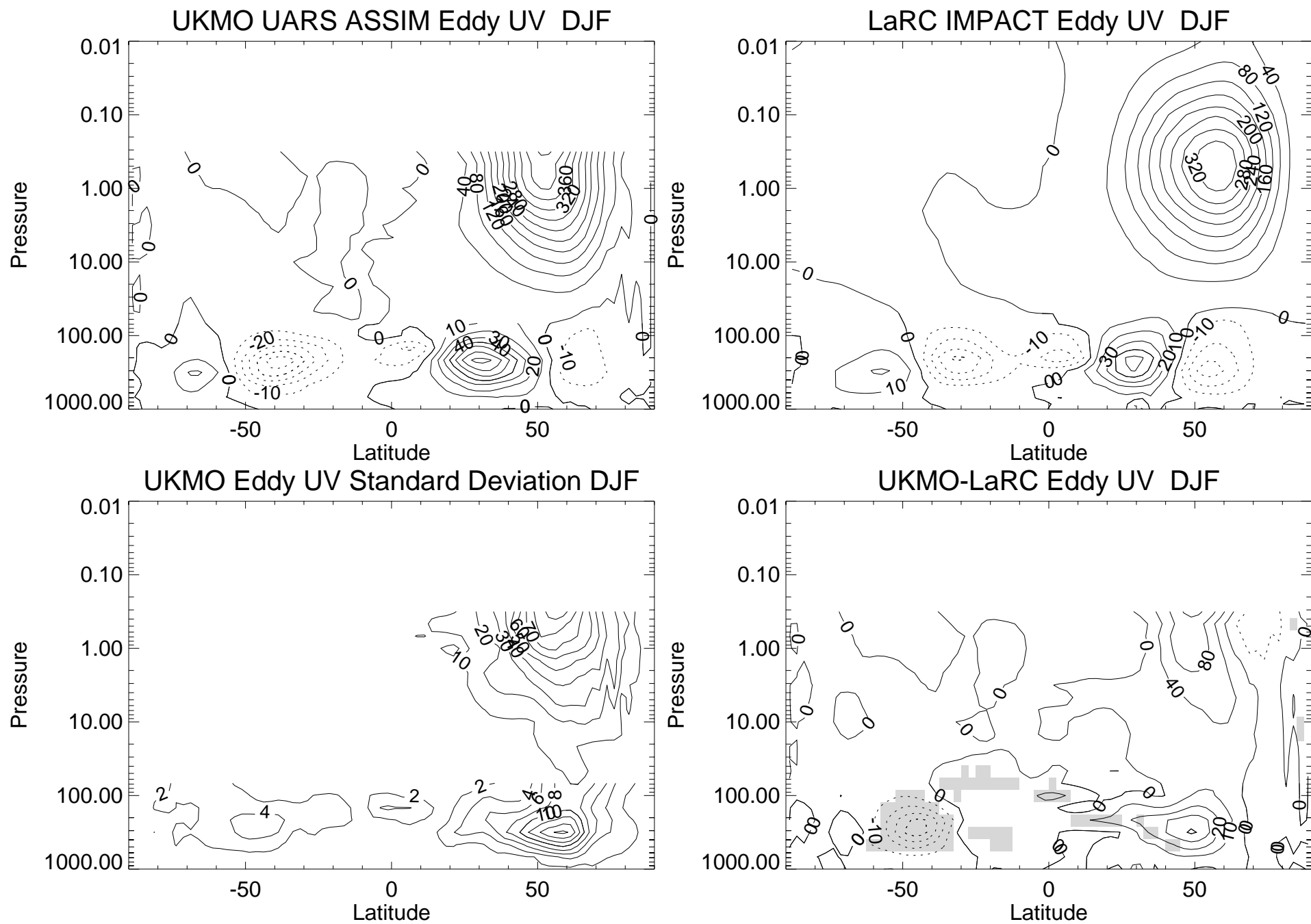


Figure 3



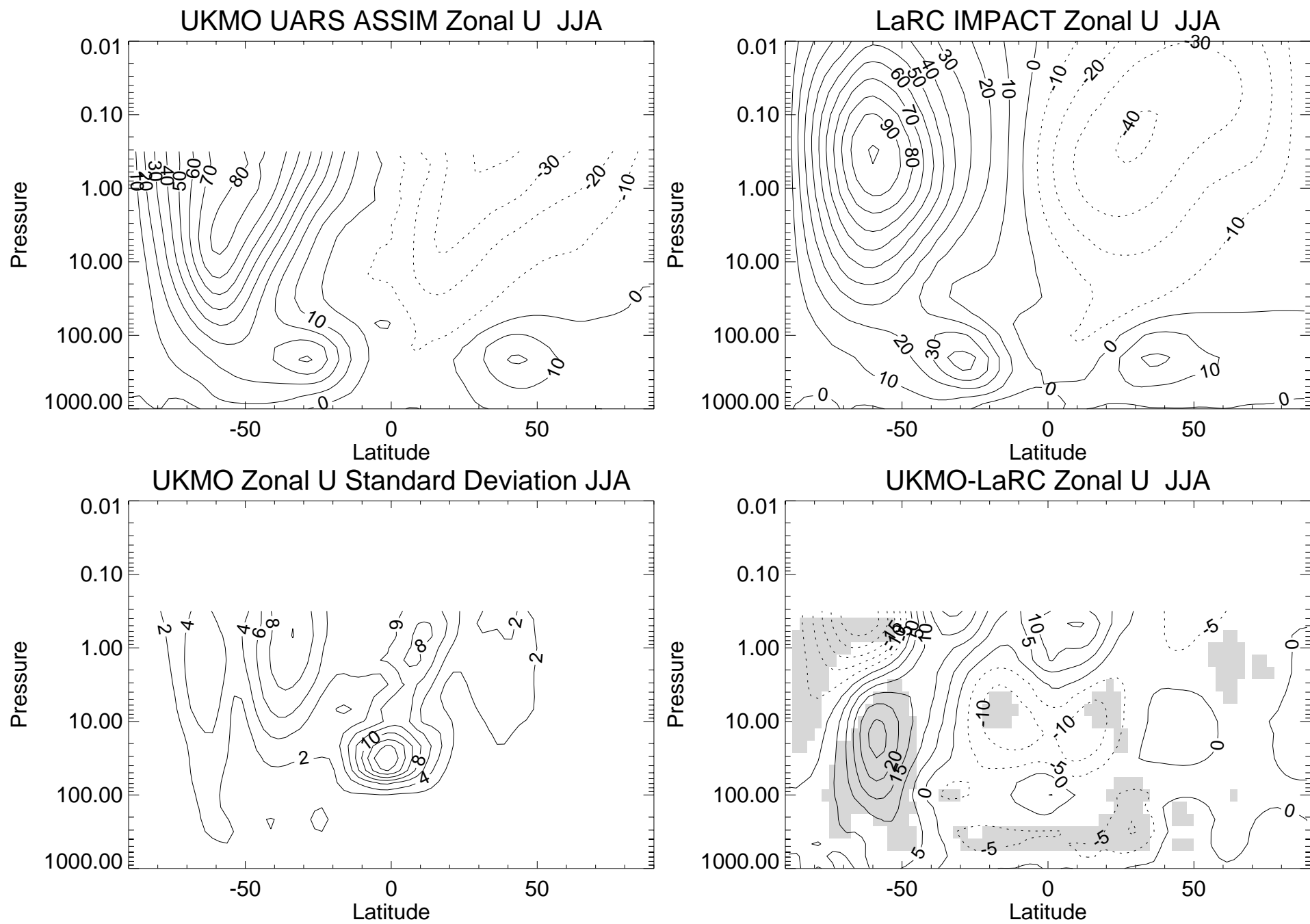


Figure 5

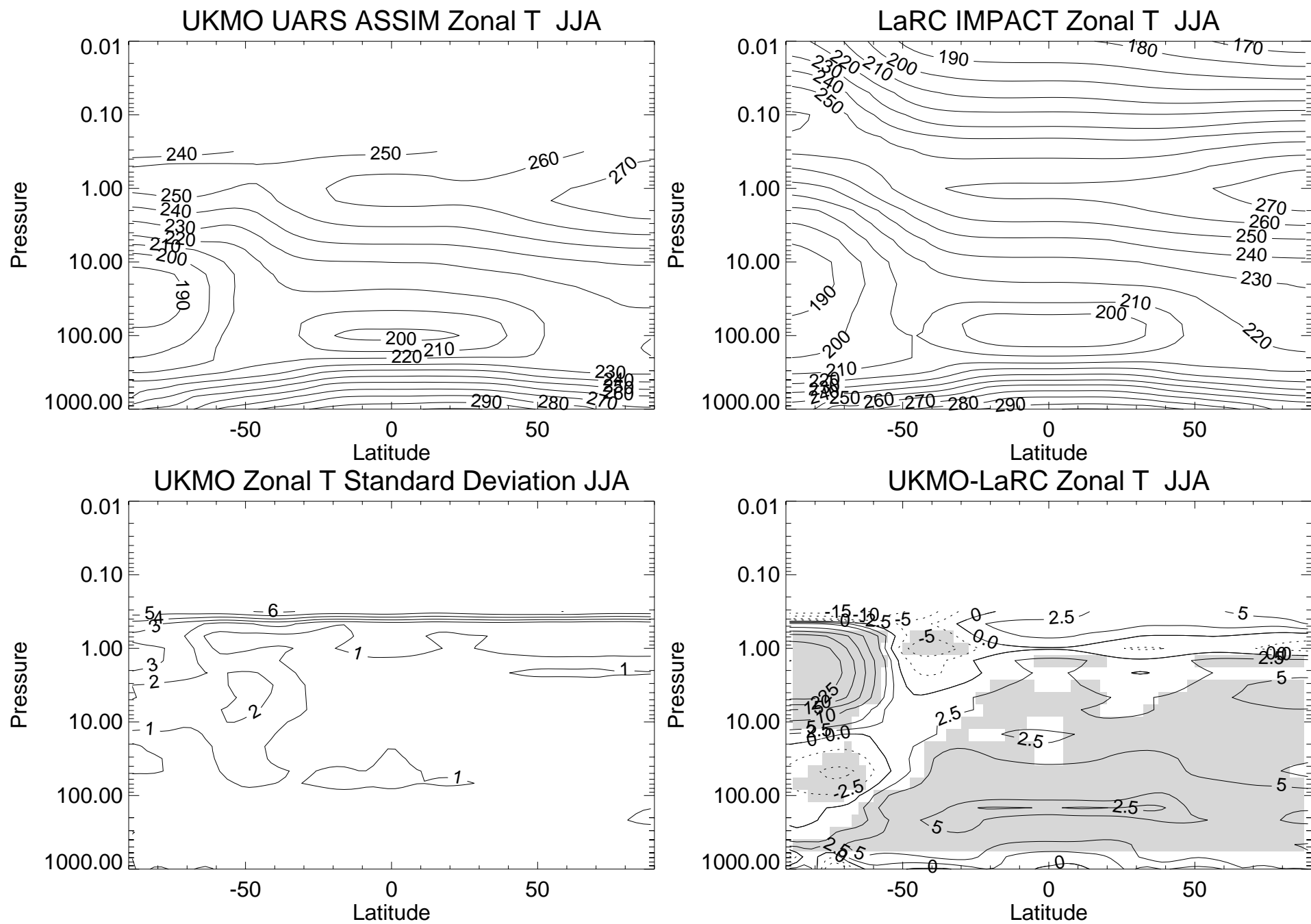


Figure 6

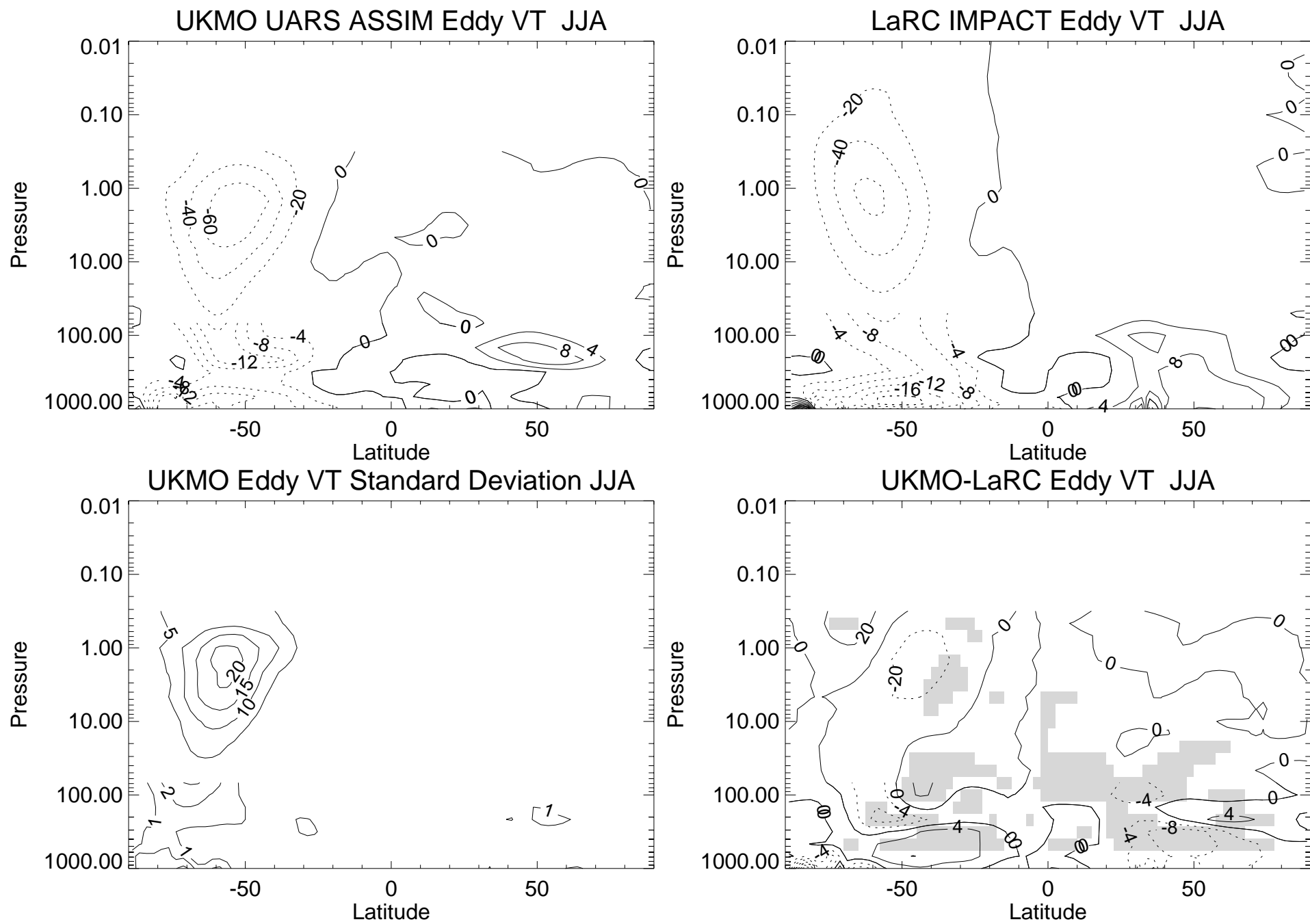


Figure 7

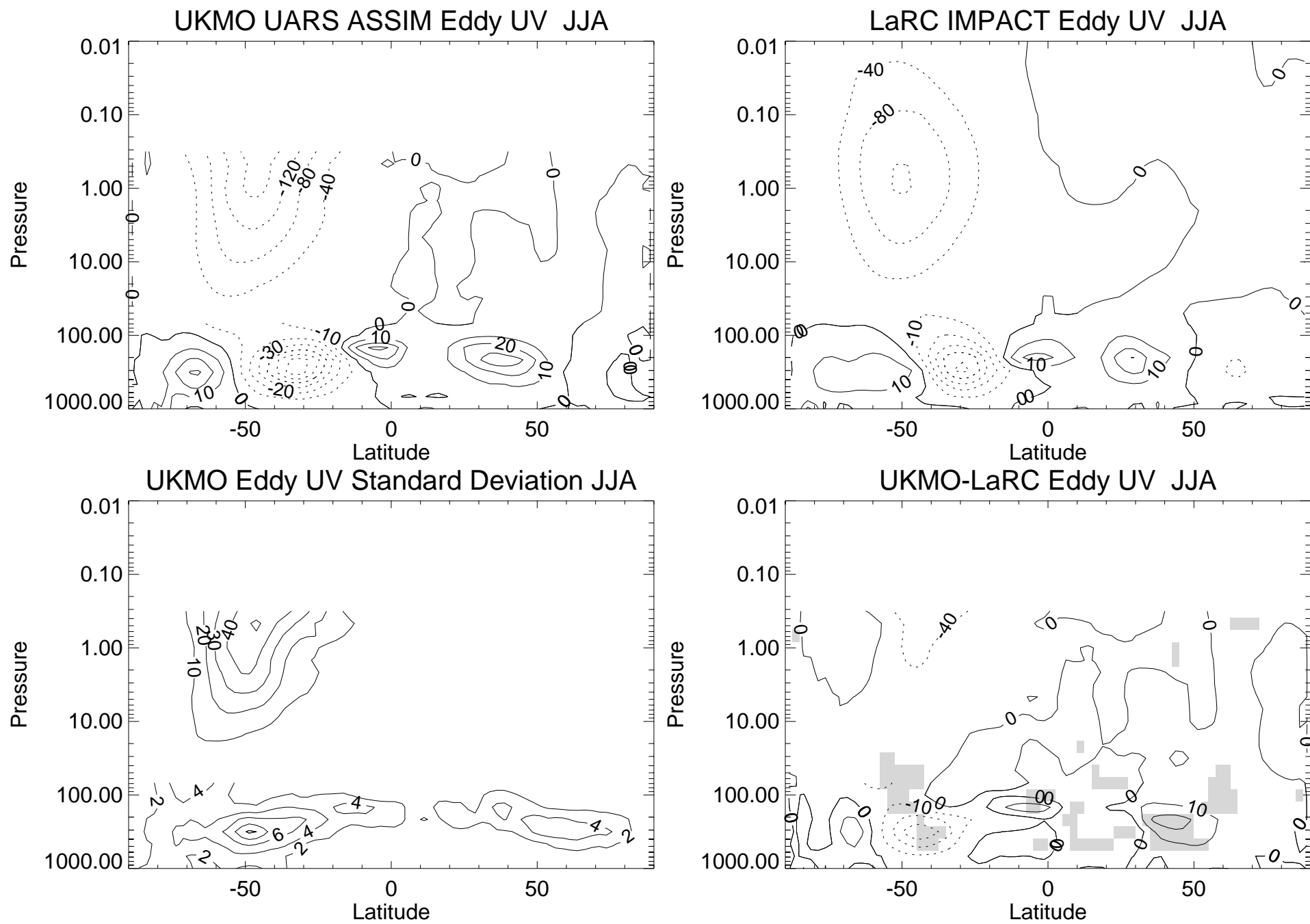


Figure 8

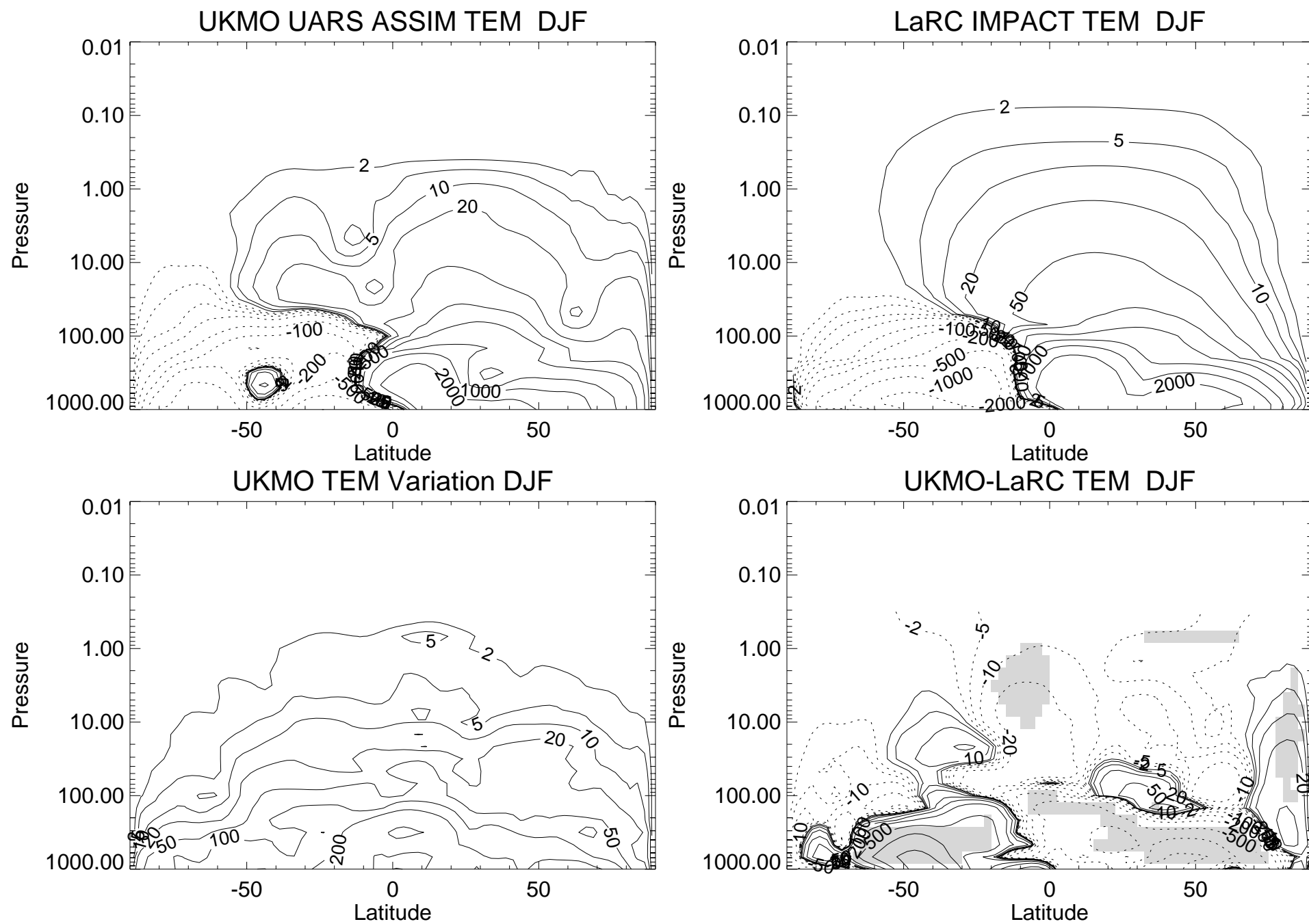


Figure 9

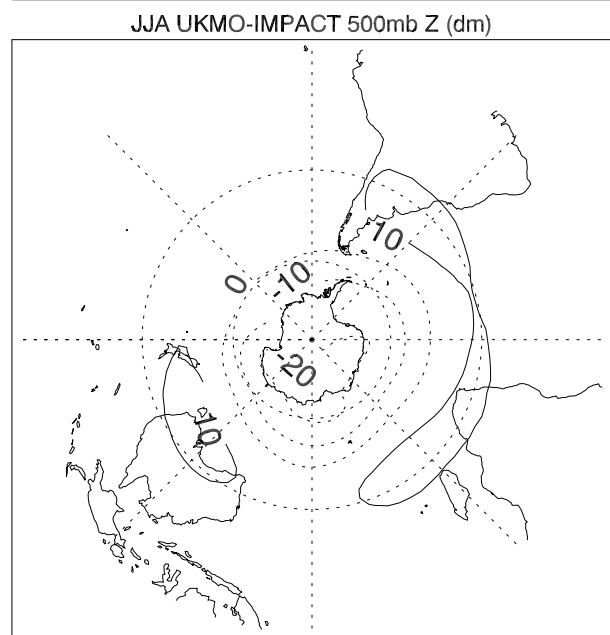
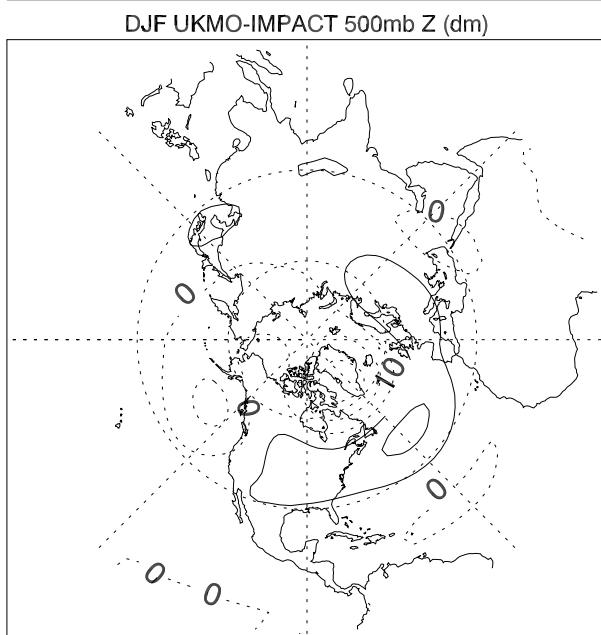
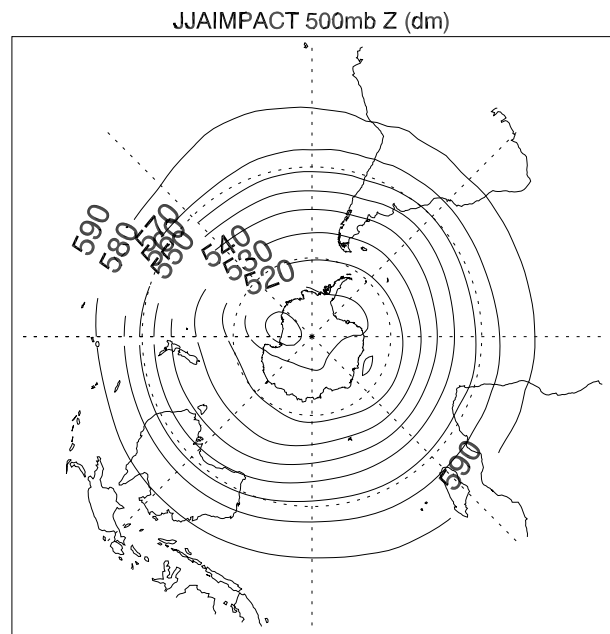
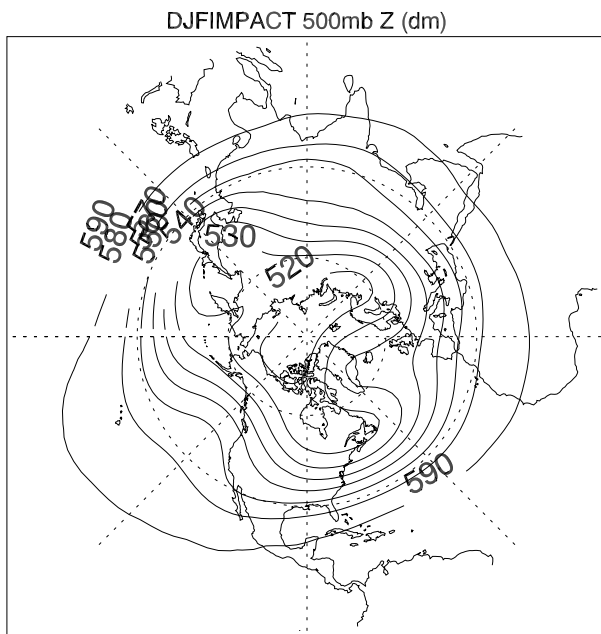
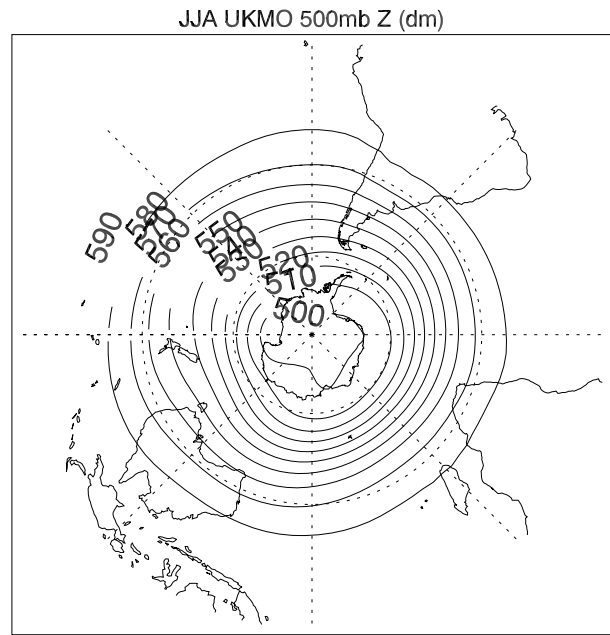
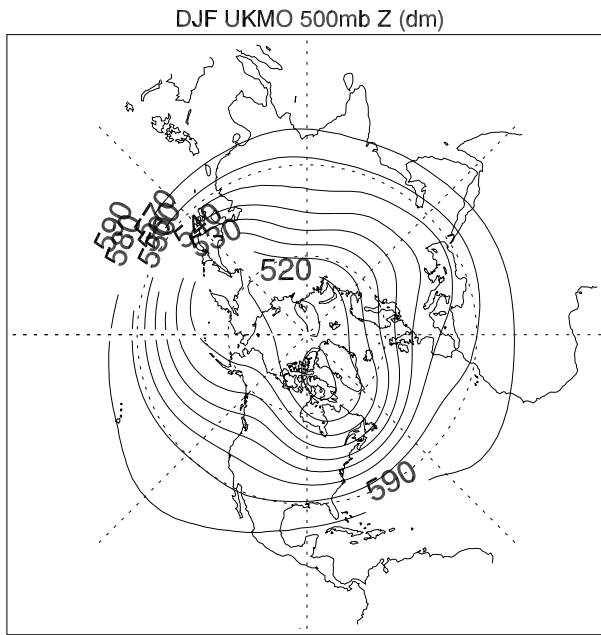


Figure 11

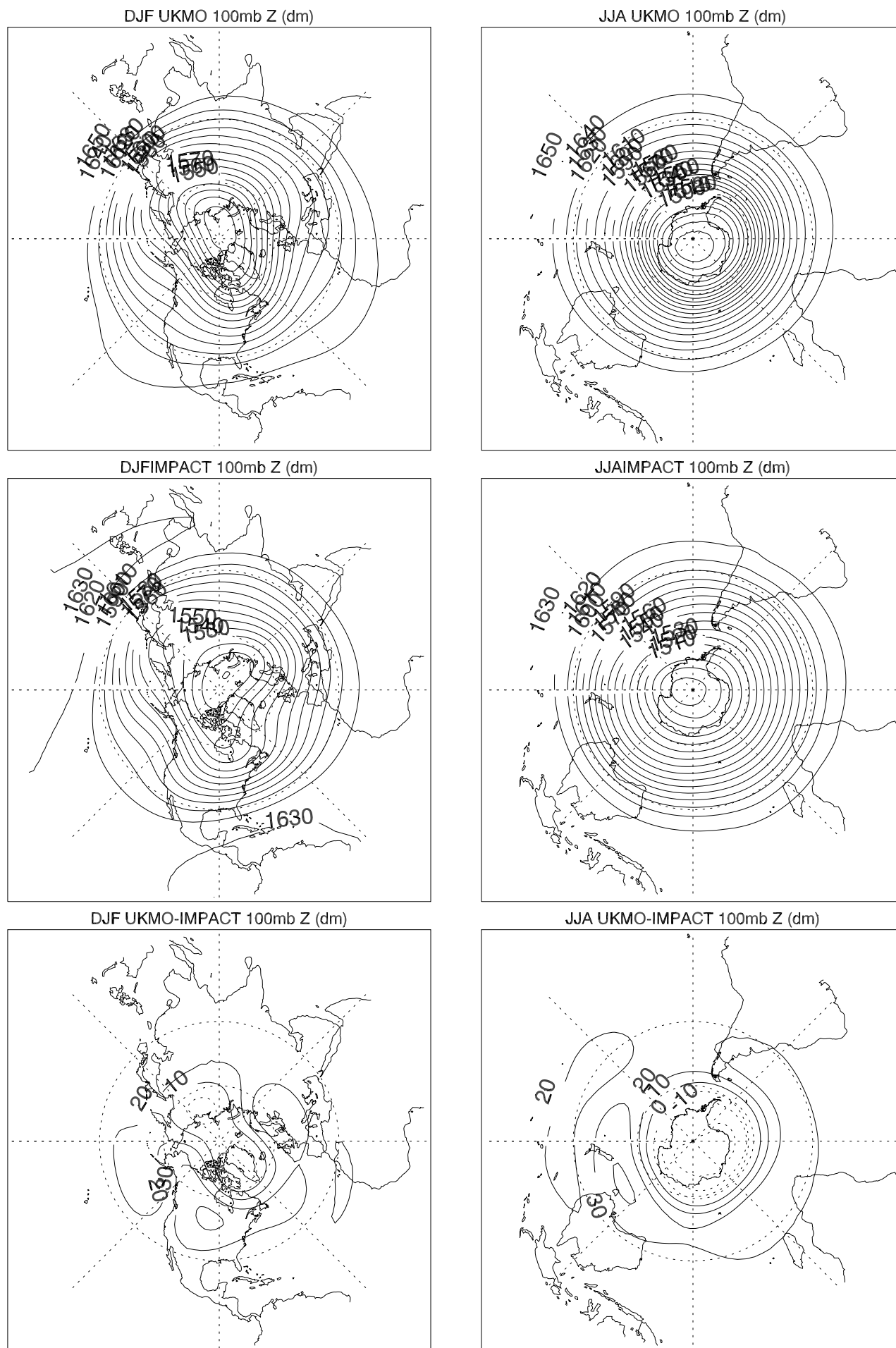


Figure 12

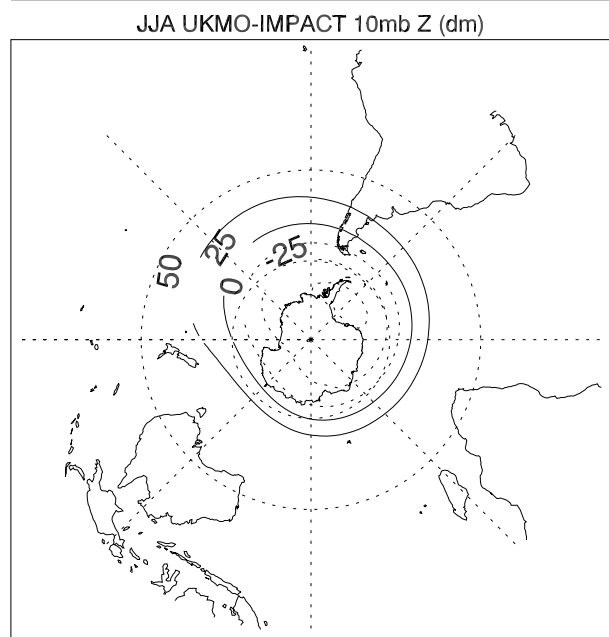
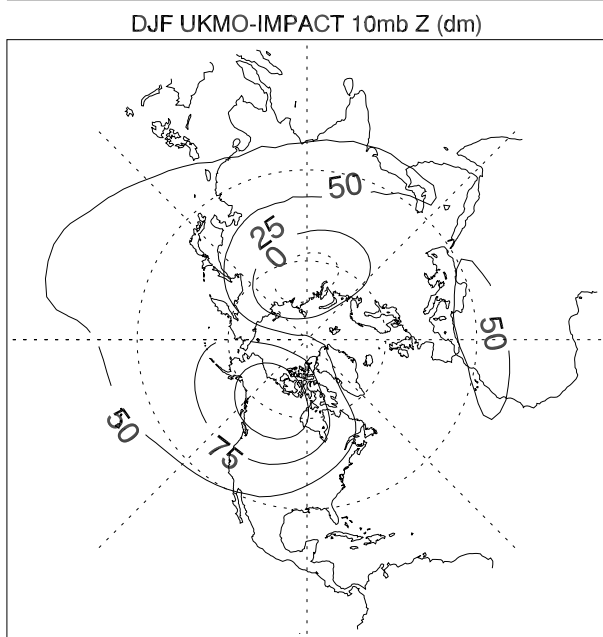
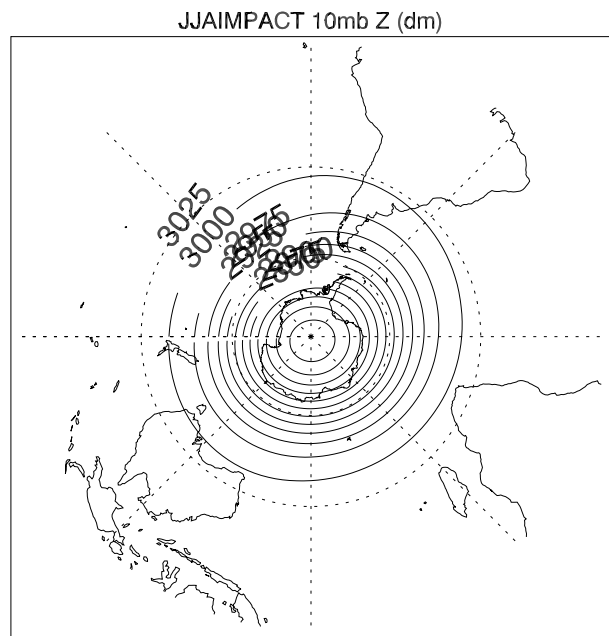
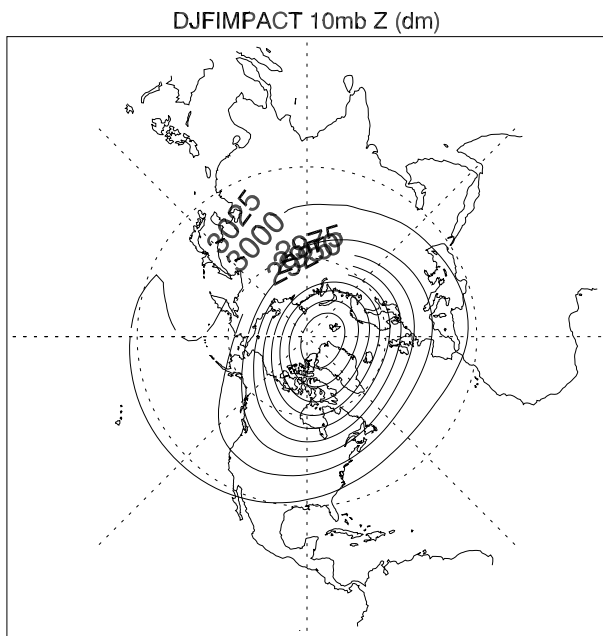
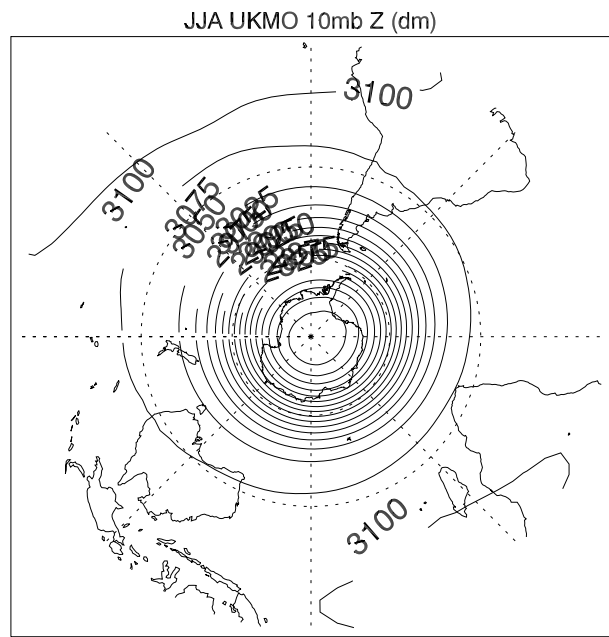
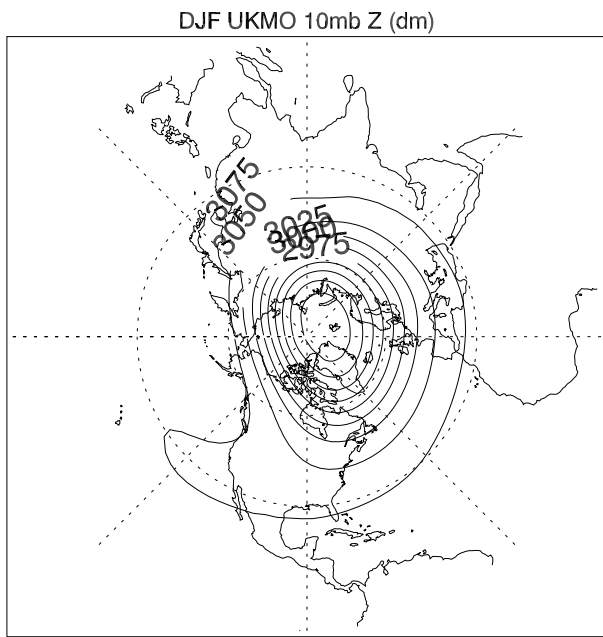


Figure 13

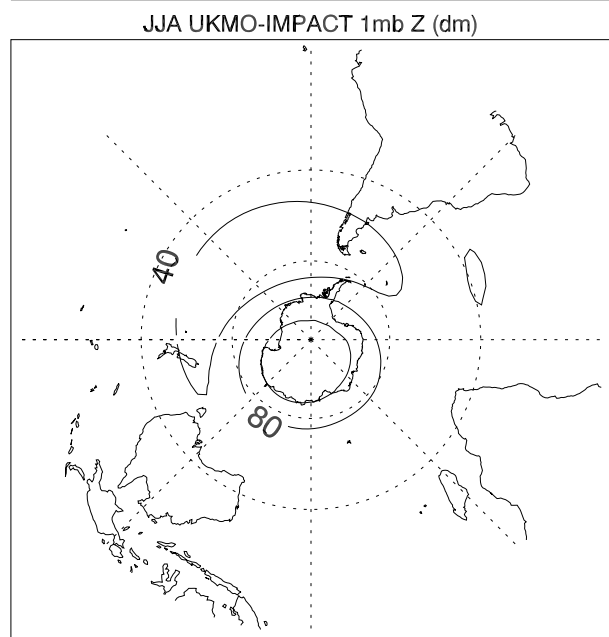
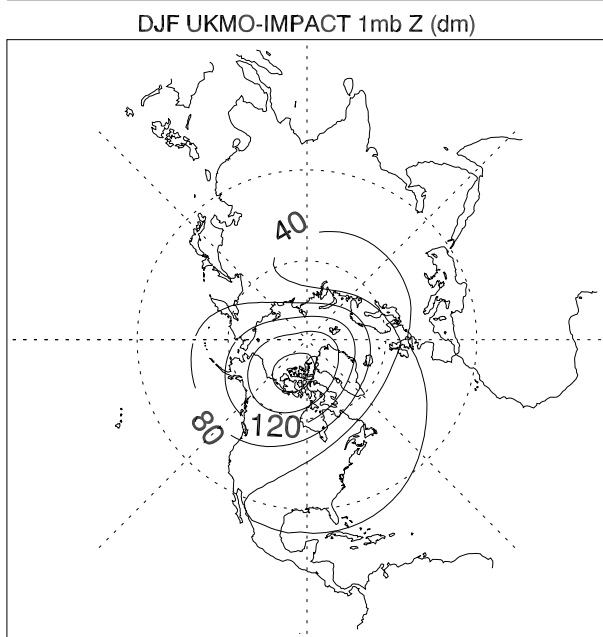
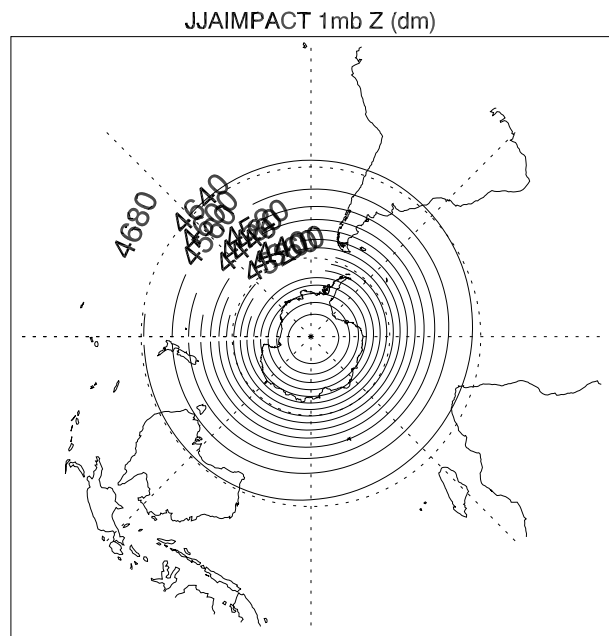
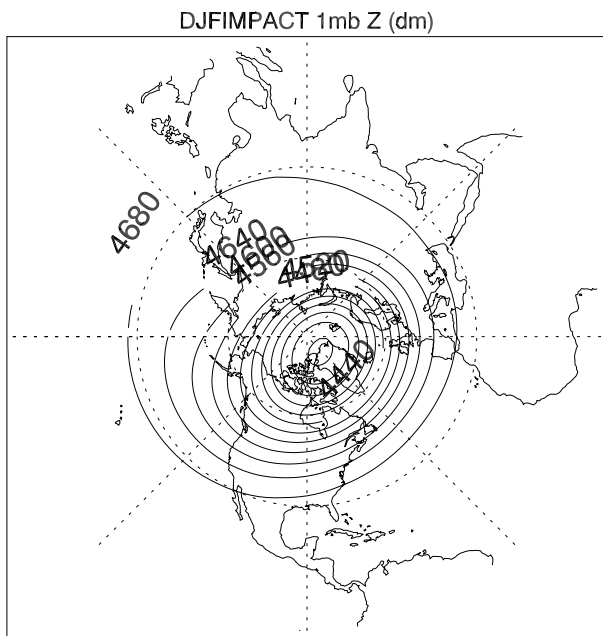
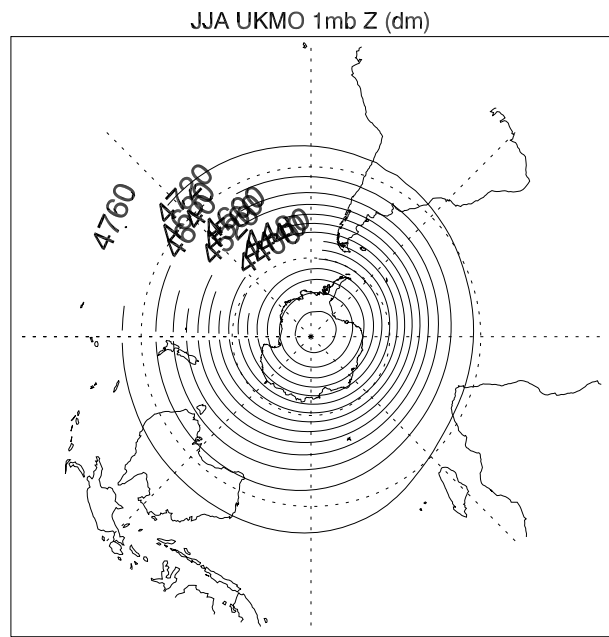
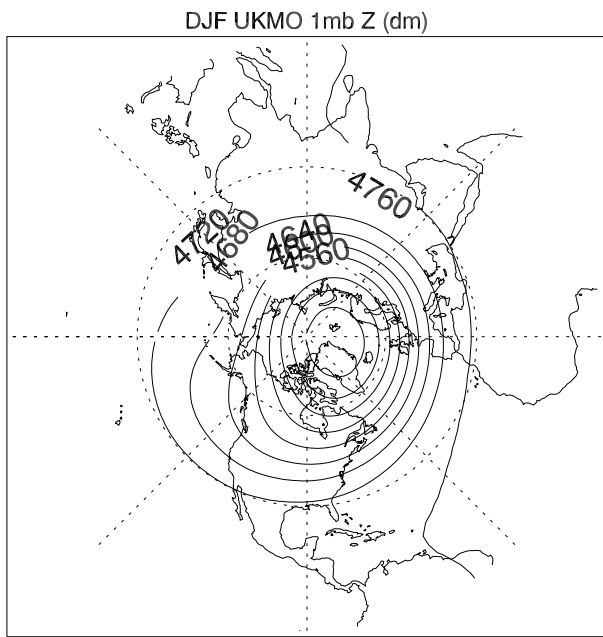
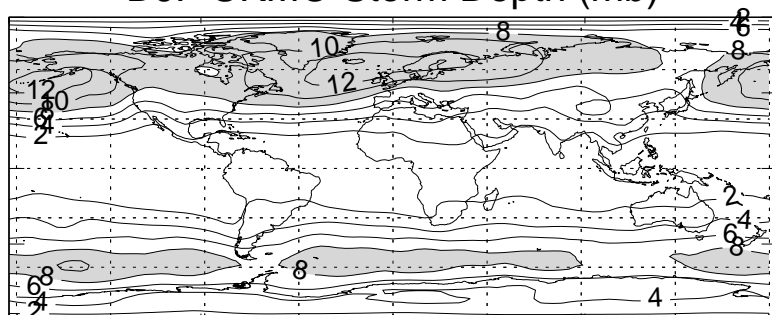
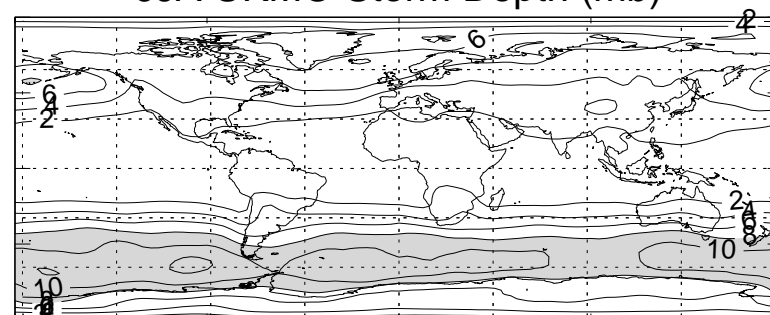


Figure 14

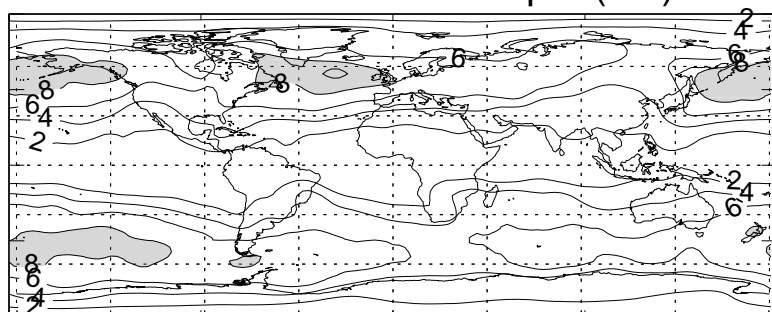
DJF UKMO Storm Depth (mb)



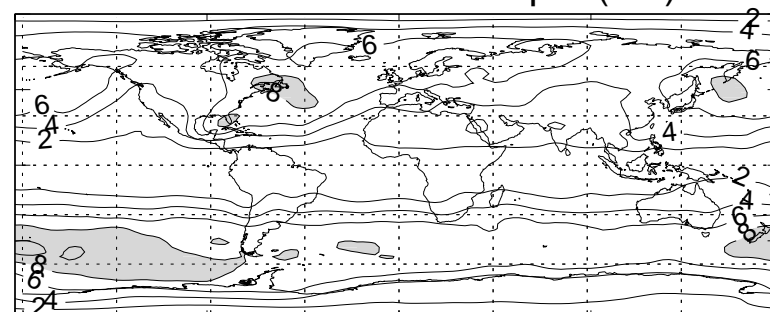
JJA UKMO Storm Depth (mb)



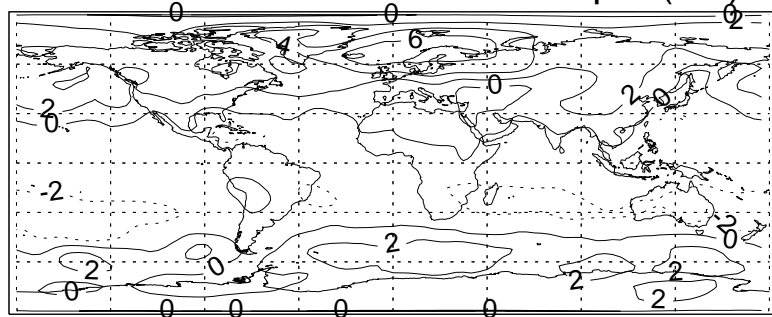
DJF IMPACT Storm Depth (mb)



JJA IMPACT Storm Depth (mb)



DJF UKMO-IMPACT Storm Depth (mb)



JJA UKMO-IMPACT Storm Depth (mb)

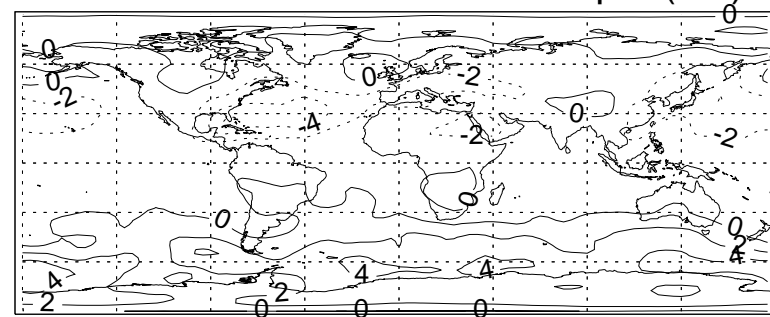
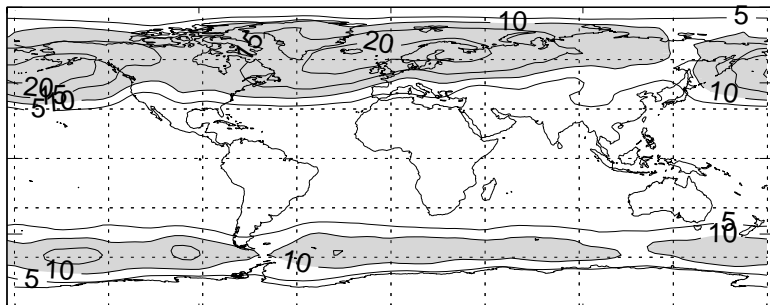
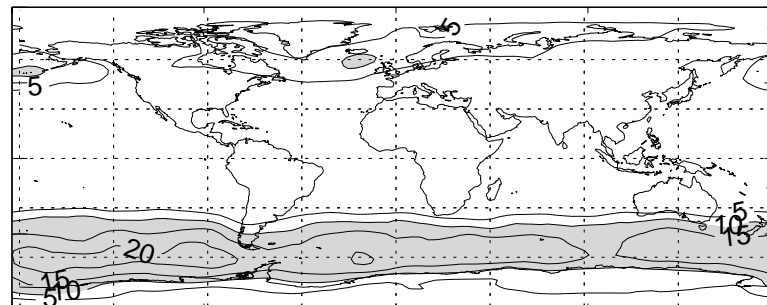


Figure 15

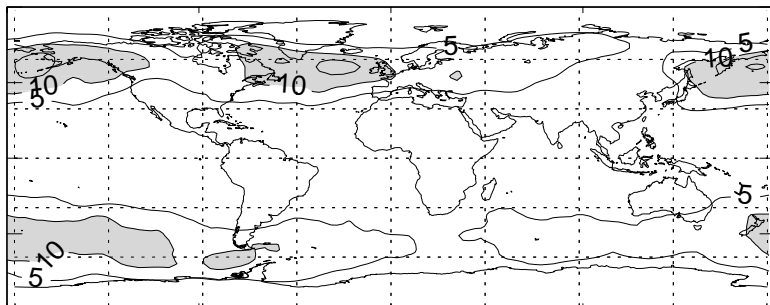
DJF UKMO Storm Frequency (%)



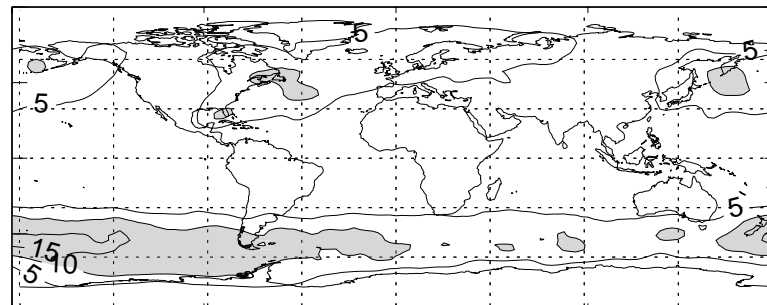
JJA UKMO Storm Frequency (%)



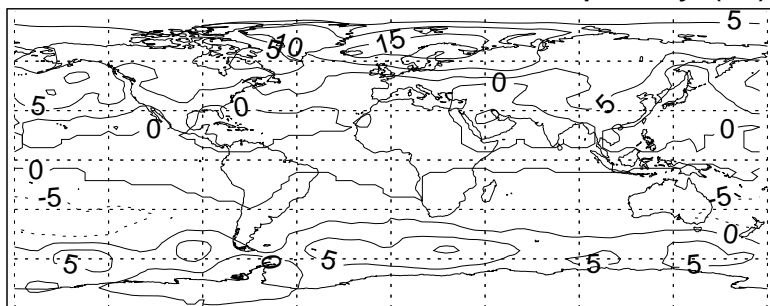
DJF IMPACT Storm Frequency (%)



JJA IMPACT Storm Frequency (%)



DJF UKMO-IMPACT Storm Frequency (%)



JJA UKMO-IMPACT Storm Frequency (%)

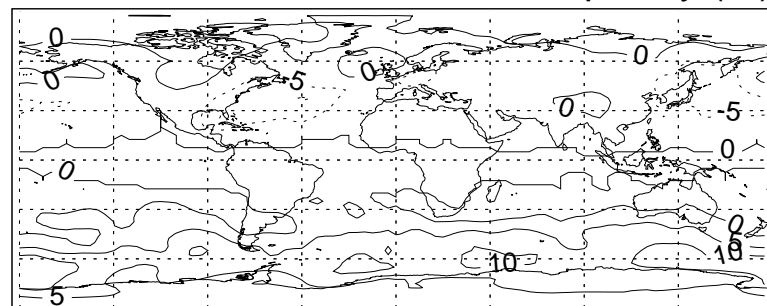
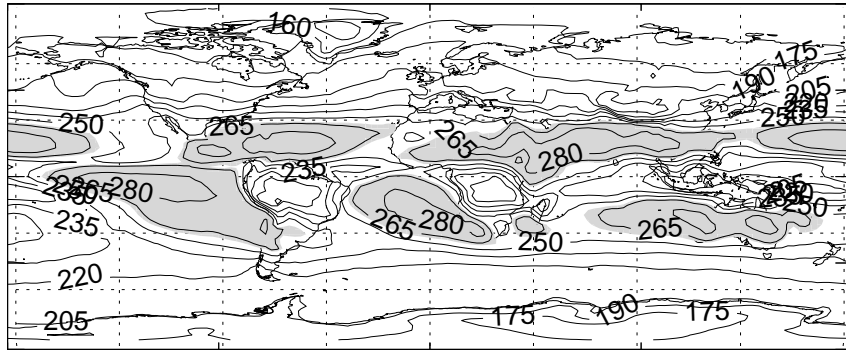
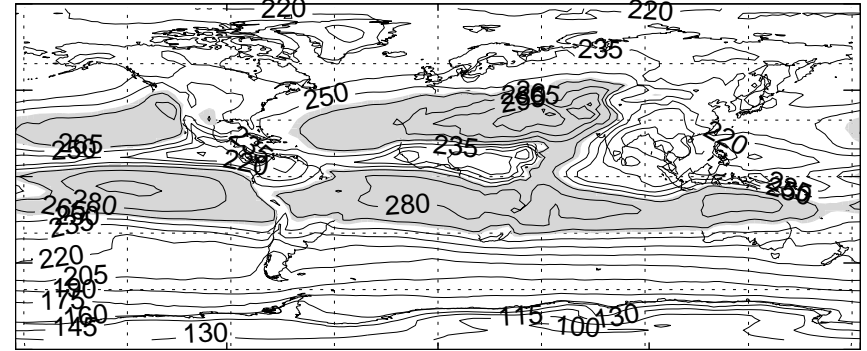


Figure 16

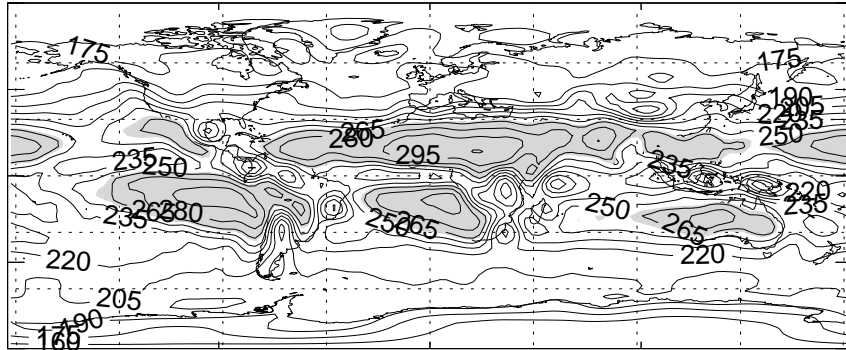
DJF ERBE OLR (W/m^2)



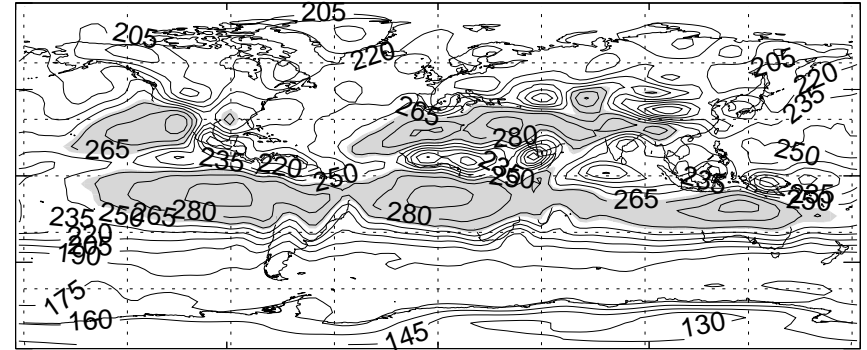
JJA ERBE OLR (W/m^2)



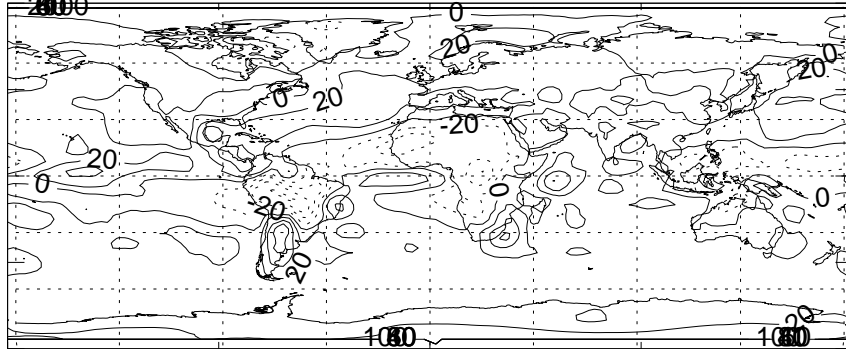
DJF IMPACT OLR (W/m^2)



JJA IMPACT OLR (W/m^2)



DJF ERBE-IMPACT OLR (W/m^2)



JJA ERBE-IMPACT OLR (W/m^2)

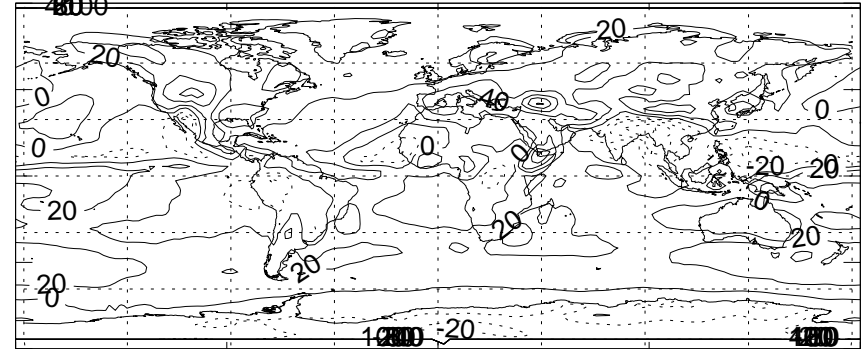
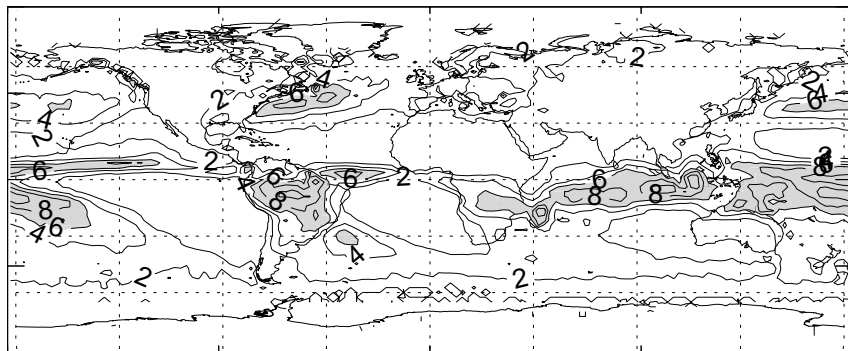
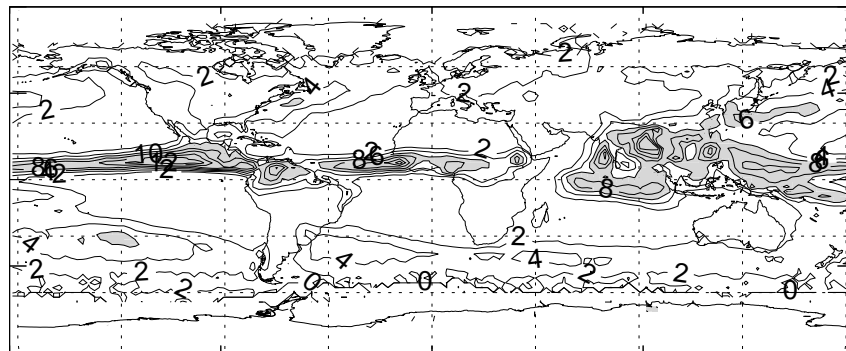


Figure 17

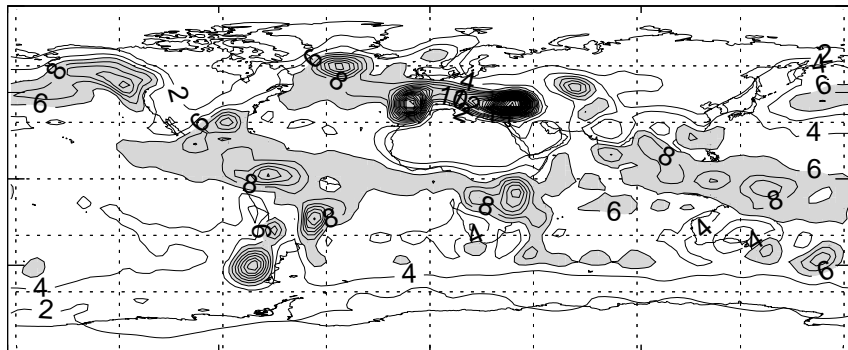
DJF GPCP Precip (mm/day)



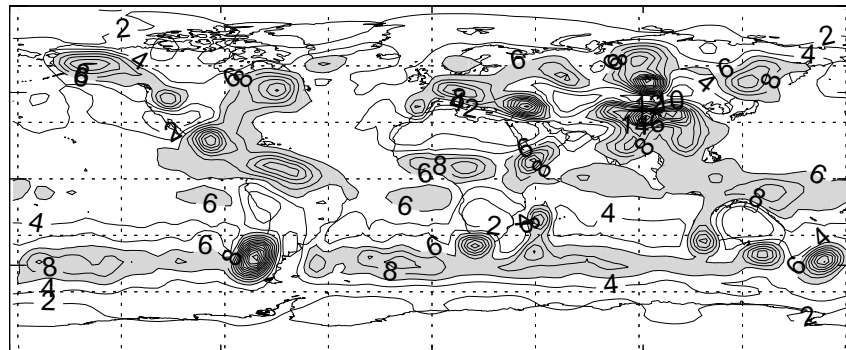
JJA GPCP Precip (mm/day)



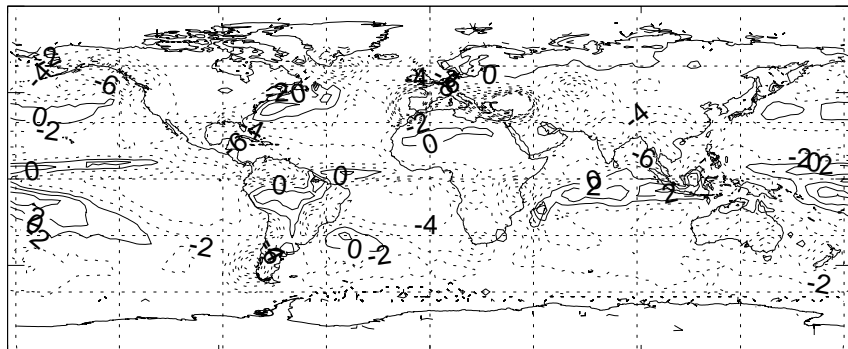
DJF IMPACT Precip (mm/day)



JJA IMPACT Precip (mm/day)



DJF GPCP-IMPACT Precip (mm/day)



JJA GPCP-IMPACT Precip (mm/day)

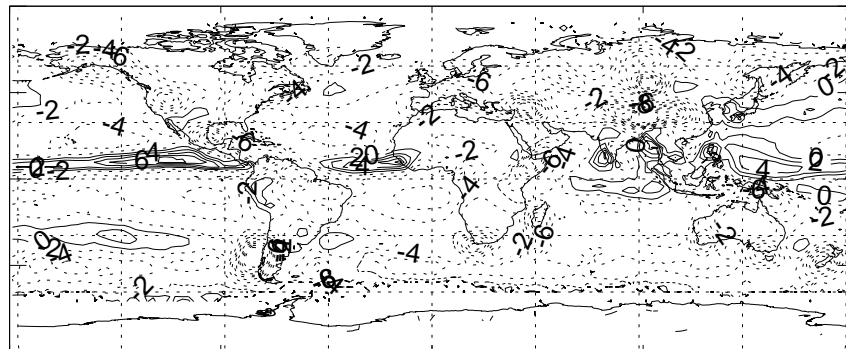
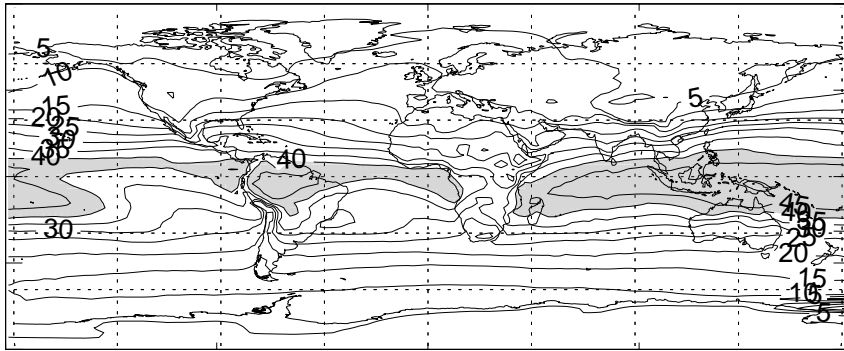
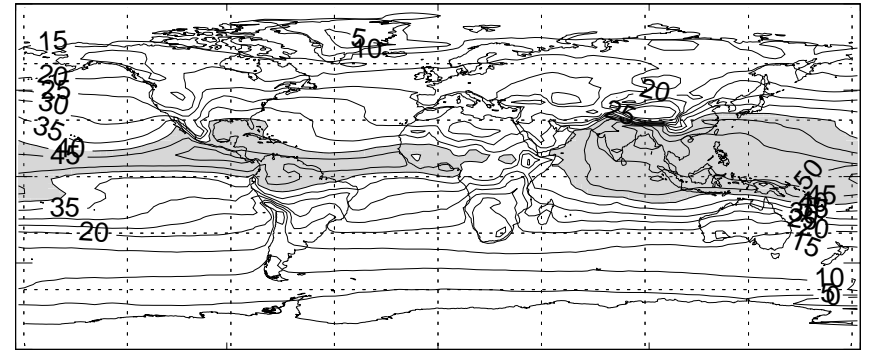


Figure 18

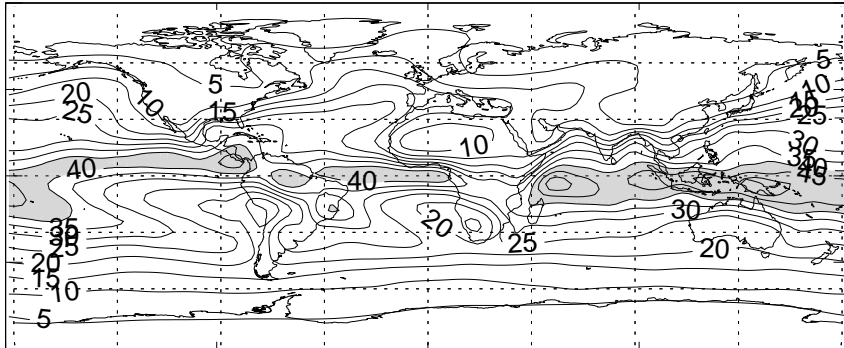
DJF ISCCP PRW (kg/m²)



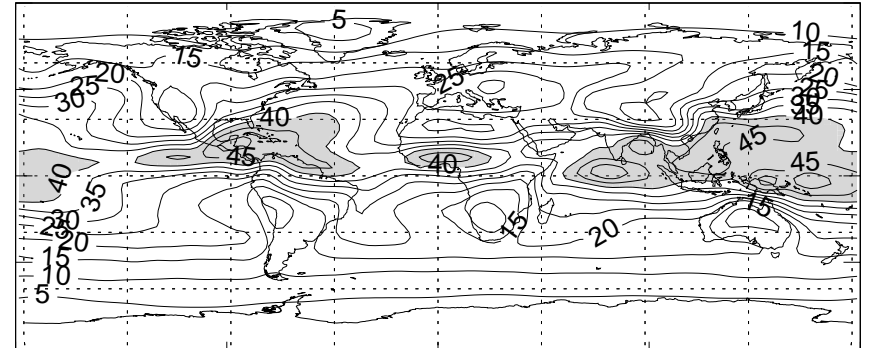
JJA ISCCP PRW (kg/m²)



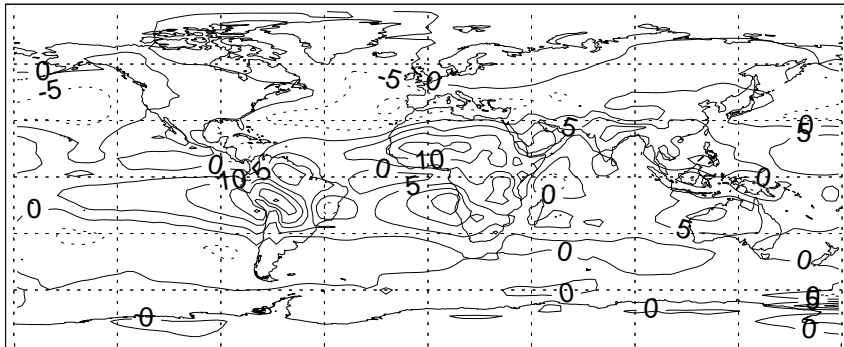
DJF IMPACT PRW (kg/m²)



JJA IMPACT PRW (kg/m²)



DJF ISCCP-IMPACT PRW (kg/m²)



JJA ISCCP-IMPACT PRW (kg/m²)

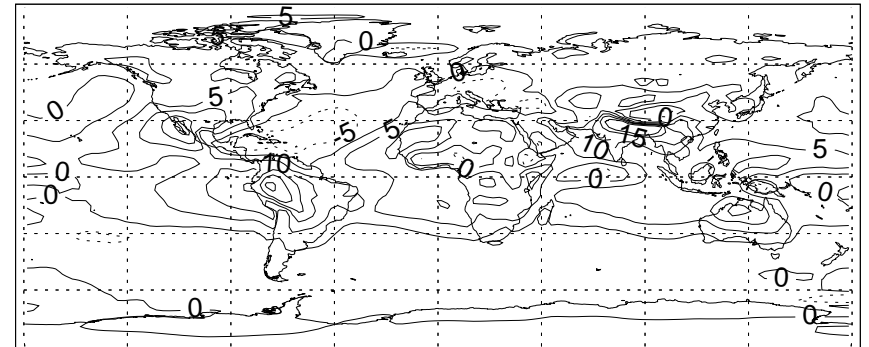
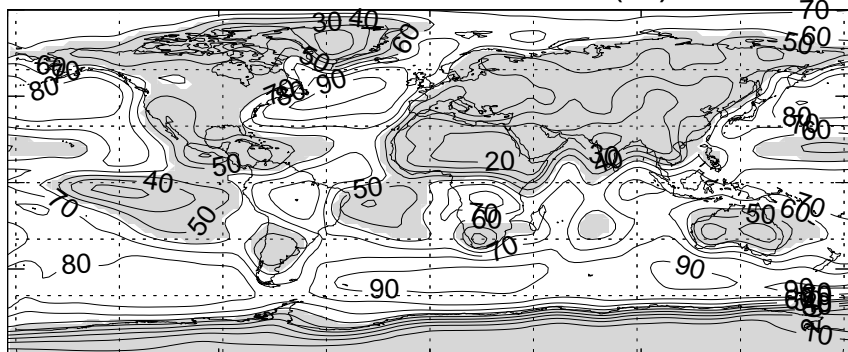
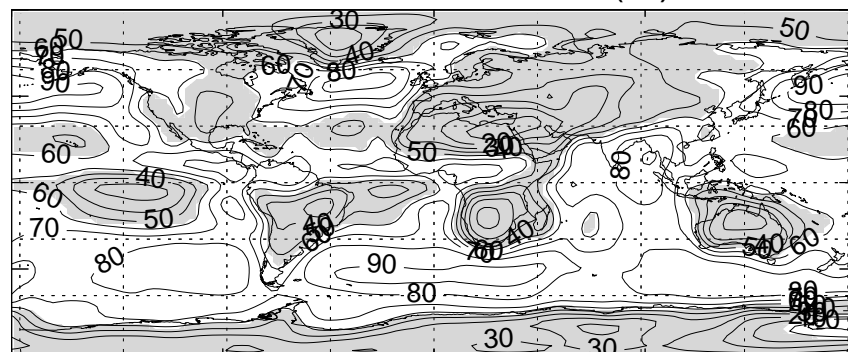


Figure 19

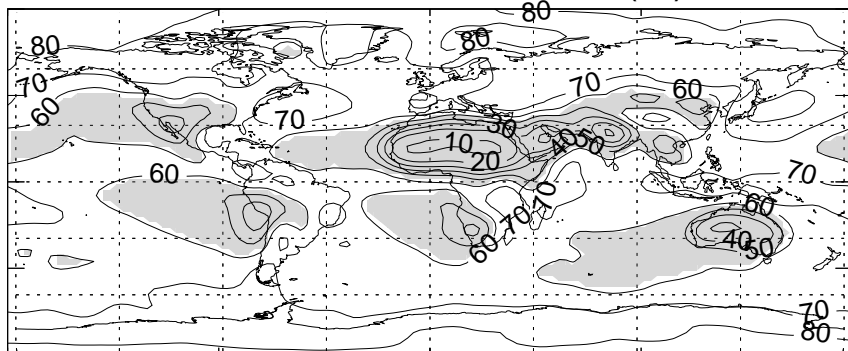
DJF ISCCP Total Cloud (%)



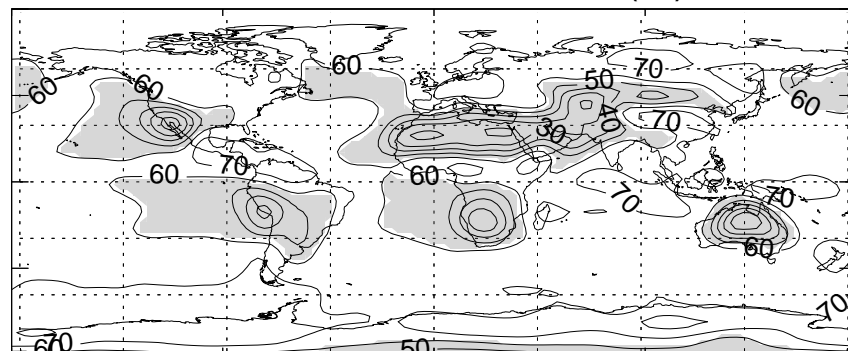
JJA ISCCP Total Cloud (%)



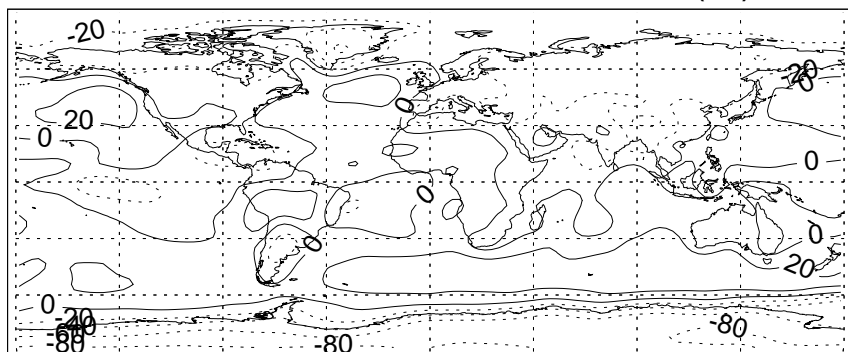
DJF IMPACT Total Cloud (%)



JJA IMPACT Total Cloud (%)



DJF ISCCP-IMPACT Total Cloud (%)



JJA ISCCP-IMPACT Total Cloud (%)

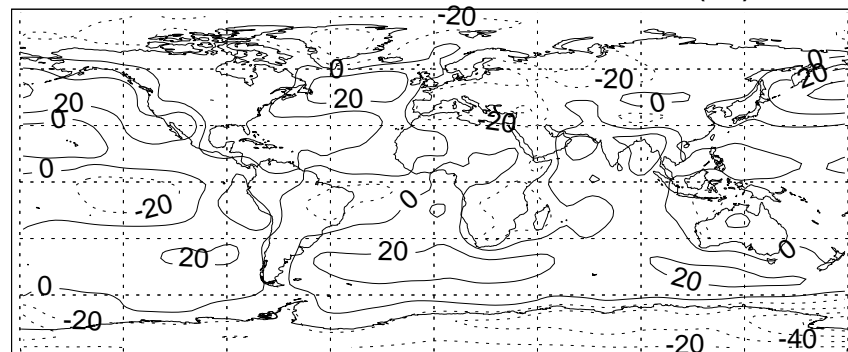


Figure 20

